APPNING2018

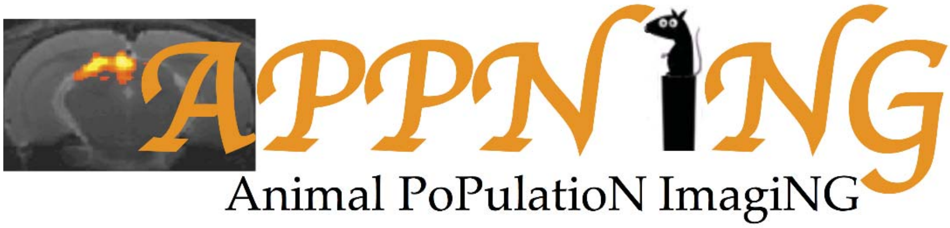

INHA, Paris – 22 June 2018

FLi France Life Imaging

GIN

BRUKER

Roche

Organization Committee

Jan G. Bjaalie, Institute of Basic Medical Sciences, Oslo, Norway

Michel Dojat, Grenoble Institut des Neurosciences, Grenoble, France

Emmanuel L. Barbier, Grenoble Institut des Neurosciences, Grenoble, France

Organization Staff

Emmanuelle Grillon, UMS IRMaGe, Grenoble, France

Program Committee

Alexandra Badea, Duke University, USA

Emmanuel L. Barbier, Grenoble Institut des Neurosciences, France

Jan Bjaalie, Institute of Basic Medical Sciences, Norway

Rembrandt Bakker, Donders Institute for Brain, Cognition and Behaviour, Netherlands

Nicolas Costes, Cermep, France

Thierry Delzescaux, Mircen, France

Michel Dojat, Grenoble Institut des Neurosciences, France

Michael Hawrylycz, Allen Institute, USA

Marc Henkelman, Mouse Imaging Centre, Canada

Sean Hill, EPFL, Switzerland

Aoki Ichio, NIRS, Japan

G. Allan Johnson, Duke University, USA

Michael Kain, Inria, France

Frank Kober, CRMBM, France

Vincent Noblet, Unistra, France

Roberto Toro, Institut Pasteur, France

Markus von Kienlin, F. Hoffmann- La Roche, Switzerland

Program

9:00	Welcome
9:25	Workshop opening - Emmanuel L. Barbier

Morning session - Moderators: Michel Dojat and Frank Kober

9:30	Quantitative Connectomic Histology, **G. Allan Johnson**, *Duke University, Durham, NC, USA*
10:15	Multi-modality and multi-level data integration through brain atlasing: Human Brain Project tools and strategies, **Jan G. Bjaalie**, *Institute of Basic Medical Sciences, Oslo, Norway*
11:00	Poster teasing session (2 minutes per teasing, 20 posters)
12:00	Lunch and poster session

Afternoon Session - Moderators: Jan G. Bjaalie and Emmanuel L. Barbier

13:30	Common Coordinate Frameworks in Animal Population Imaging, **Michael Hawrylycz**, *Allen Institute for Brain Science, Seattle, USA*
14:15	The Boon and Bane of Animal Population Imaging - A Pharma Industry's Perspective, **Basil Künnecke**, *Roche Innovation Center, Basel, Switzerland*
15:00	Coffee break
15:15	Automating image processing with machine learning, **Anna Kreshuk**, *Interdisciplinary Center for Scientific Computing, Heidelberg, Germany*
16:00	Industry corner
	Advances in preclinical imaging of small rodents: Technology & Applications, **Claire Wary**, *Bruker Biospin, Ettlingen, Germany*
	Translational Imaging @ Roche: Remit, Implementation and Value of Preclinical MRI, **Basil Künnecke**, *Roche Innovation Center, Basel, Switzerland*
16:15	Round table: Challenges for population imaging in animal studies?
17:00	**End of the workshop**

Posters

1. SBA Composer: web-based software for exploring brain slices, volumes and surfaces in a 3D atlasing context

Bakker Rembrandt (1) (2), Osoianu Anastasia (2), øvsthus Martin (3), Leergaard Trygve (3), Tiesinga Paul (2)

1 - Inm6 (Germany), **2.** Neuroinformatics (Netherlands), 3 - Oslo anatomy (Norway)

2. The electronic collection of vertebrate brains of the National Natural History Museum of Paris

Heuer Katja (1), Toro Roberto (1), Santin Mathieu (2), Herbin Marc (3), Valabregue Romain (2)

1. Institut Pasteur [Paris], **2.** Institut du Cerveau et de la Moëlle Epinière = Brain and Spine Institute [Paris], 3 - Muséum National d'Histoire Naturelle [Paris] (France)

3. Towards a connectome atlas of the C57Bl6 mouse brain using ex vivo ultra-high field diffusion MRI

Uszynski Ivy (1) (2), Mathieu Hervé (1) (4), Deloulme Jean-Christophe (1), Barbier Emmanuel (1), Poupon Cyril (3)

1. Grenoble Institut des Neurosciences, **2.** UNIRS, Saclay, 3 - IRMaGe - Biomédicale et neurosciences [Grenoble] (France)

4. Surface-based cortical parcellation and atlas creation of the sheep brain

Love Scott (1), Siwiaszczyk Marine (1), Destrieux Christophe (2), Andersson Frédéric (2), Chaillou Elodie (1)

1. INRA [Tours] (France), **2.** iBrain (France)

5. Construction of an MRI-Based Connectome for the Marmoset Brain: Methods and Initial Results

Yen Cecil (1), Liu Cirong (1), Sczupak Diego (1), Marcelle Madeline (1), Silva Afonso (1)

1. National Institutes of Health [Bethesda, MA] (United States)

6. Sharing research imaging data in « Imageries du Vivant ». An ongoing experience at Sorbonne Paris Cité University (SPC)

Abidi L. (1), Garteiser P. (1), Cerin C. (1), Smadja M. (2), Sahri S. (1), Bentounsi M. (1), Geldwerth D. (1), Li-Thiao-Té S. (1), Frapart Y.-M. (1),

1. 1Sorbonne Paris cité University, Paris (France), **2.** SisNcom (France)

7. Sammba-MRI: An imaging toolbox for small animal imaging by MRI

Bougacha Salma (1) (2), Nadkarni Nachiket (1), Garin Clément (1), Dhenain Marc (1)

1. Laboratoire des Maladies Neurodégénératives - UMR 9199 [Fontenay-Aux-Roses] (France), **2.** Neuropsychologie et imagerie de la mémoire humaine [Caen] (France)

8. Dicomifier: a generic Bruker-DICOM-NIfTI converter

Lamy Julien (1), Lahaxe Romain (1), Ouhmich Farid (1)

1. Laboratoire des sciences de l'ingénieur, de l'informatique et de l'imagerie [Strasbourg] (France)

9. FLI-Image Analysis and Management

Kain Michael (1) and the France Life Imaging (FLI) Consortium

1. Inria Rennes, Bretagne Atlantique [Rennes] (France)

10. Development of a configurable workflow for processing preclinical images

Zullino Sara (1), Dastrù Walter (1), Aime Silvio (1), Longo Dario (1)

1. Molecular Imaging Center, Dept. Molecular Biotechnologies and Health Sciences, University of Torino (Italy)

11. Multi-centre resting-state fMRI comparison reveals common functional networks in the mouse brain

Grandjean Joanes (1), Canella Carola (2) (3), Anckaerts Cynthia (4), Ayranc? Gülebru (5), Coletta Ludovico (2) (3), Gallino Daniel (5), Gass Natalia (6), Hübner Neele (7), Kreitz Silke (8), Mandino Francesca (1) (9), Mechling Anna (7), Strobelt Sandra (8), Wu Tong (10) (11), Wank Isabel (8), Yeow Ling Yun (1), Yee Yohan (12), Chakravarty Mallar (5), Chang Wei-Tang (1), Von Elverfeldt Dominik (7), Harsan Laura-Adela (13), Hess Andreas (8), Keliris Georgios (4), Lerch Jason (12), Rudin Markus (14) (15), Sartorius Alexander (6), Jiang Tianzi (10) (16), Van Der Linden Annemie (4), Verhoye Marleen (4), Weber-Fahr Wolfgang (6), Wenderoth Nicole (17), Zerbi Valerio (17), Gozzi Alessandro (2)

1. Singapore Bioimaging Consortium, Agency for Science, Technology and Research (Singapore), **2.** Functional Neuroimaging Laboratory, Istituto Italiano di Tecnologia, centre for Neuroscience and Cognitive Systems @ UNITN (Italy), **3.** CIMeC, centre for Mind/Brain Sciences, University of Trento (Italy), **4.** Bio-Imaging Lab, University of Antwerp (Belgium), **5.** Douglas Mental Health University Institute & Departments of Psychiatry and Biological and Biomedical Engineering, McGill University (Canada), **6.** Department of Neuroimaging, Central Institute of Mental Health, Medical Faculty Mannheim, University of Heidelberg (Germany), **7.** Advanced Molecular Imaging Research centre (AMIR), Medical Physics, Department of Radiology, University Medical centre and the BrainLinks-BrainTools Cluster of Excellence, University of Freiburg (Germany), **8.** Institute of Experimental and Clinical Pharmacology and Toxicology, Friedrich-Alexander University Erlangen-Nürnberg (FAU) (Germany), **9.** Faculty of Life Sciences, University of Manchester (United Kingdom), **10.** Queensland Brain Institute, The University of Queensland (Australia), **11.** Centre for Medical Image Computing, Department of Computer Science, &

Max Planck University College London Centre for Computational Psychiatry and Ageing Research, University College London (United Kingdom), **12.** Hospital for Sick Children (Canada), **13.** Department of Biophysics and Nuclear Medicine, University Hospital Strasbourg (France), **14.** Institute for Biomedical Engineering, University and ETH Zürich (Switzerland), **15.** Institute of Pharmacology and Toxicology, University of Zürich (Switzerland), **16.** Brainnetome Centre, Institute of Automation, Chinese Academy of Sciences, Beijing & Key Laboratory for NeuroInformation of the Ministry of Education, School of Life Science and Technology, University of Electronic Science and Technology of China (China), **17.** Neural Control of Movement Lab, Department of Health Sciences and Technology, ETH Zürich (Switzerland)

12. Multi-center quantitative mapping of T1 and T2 relaxation times in the rat brain

Deruelle Tristan (1), Perles-Barbacaru Adriana (2), Kober Franck (2), Delzescaux Thierry (3), Barbier Emmanuel L. (1), Dojat Michel (1)

1. Grenoble Institut des Neurosciences [Grenoble], **2.** Aix-Marseille Univ, CNRS, CRMBM [Marseille], **3.** UMR-9199, CNRS, CEA-MIRCEN [Fontenay-Aux-Roses] (France)

13. Impact of perfusion level on the amplitude of resting-state BOLD fMRI in anesthetized rats

Becq Guillaume (1), Achard Sophie (1), Habet Tarik (2), Collomb Nora (3), Faucher Margaux (2), Delon-Martin Chantal (2), Coizet Véronique (2), Barbier Emmanuel L. (2)

1. GIPSA-Lab [Grenoble], **2.** Grenoble Institut des Neurosciences [Grenoble], **3.** IRMaGe [Grenoble] (France)

14. Long distance plasticity of callosal connections: From men to mice

Szczupak Diego (1) (2), Liu Cirong (2), Yen Cecil (2), Ferreira Fernanda (3), Lima Caroline (3), Lent Roberto (3) (1), Silva Afonso (2), Tovar-Moll Fernanda (3) (1)

1. Federal University of Rio de Janeiro (Brazil), **2.** National Institutes of Health (United States), **3.** Institute D'or Research and Education (Brazil)

15. fMRI Visual Responses of a Rat Model of Parkinson's Disease

Bellot Emmanuelle (1), Pautrat Arnaud (1), Collomb Nora (2), Montignon Olivier (2), Coizet Véronique (1), Dojat Michel (1)

1. Grenoble Institut des Neurosciences [Grenoble], **2.** IRMaGe [Grenoble] (France)

16. Monitoring glioma heterogeneity during tumor growth using clustering analysis of multiparametric MRI data

Lemasson Benjamin (1), Collomb Nora (3), Arnaud Alexis (2), Forbes Florence (2), Barbier Emmanuel L. (1)

1. Grenoble Institut des Neurosciences [Grenoble], **2.** MISTIS [Grenoble], **3.** IRMaGe [Grenoble] (France)

17. Using Imaging to Better Understand the Genetic Control of Brain Circuit Vulnerability in Mouse Models of Alzheimer's Disease

Badea Alexandra (1), Wang Michele (2) (1), Anderson Robert (1), Qi Yi (1), Cofer Gary (1), Wang Nian (1), Wang Shangsi (3), Vogelstein Joshua (4) (5), Priebe Carey (5) (3), Wilson Joan (6), Colton Carol (6)

1. Center for In Vivo Microscopy, Department of Radiology, Duke University Medical Center, **2.** Neuroscience Program, Trinity College, Duke University **3.** Department of Applied Mathematics and Statistics, Johns Hopkins University, **4.** Department of Biomedical Engineering and Institute for Computational Medicine, **5.** Center for Imaging Science, Johns Hopkins University, **6.** Neurology Department, Duke University Medical Center (United States)

18. Neuroimaging in an Autism Related Mouse Population

Ellegood Jacob (1), Henkelman Mark (1) (2), Lerch Jason (1) (2)

1. Mouse Imaging Centre, Hospital for Sick Children [Toronto], **2.** Department of Medical Biophysics, University of Toronto [Toronto] (Canada)

19. Glial and axonal changes in the cuprizone mouse model investigated with diffusion-weighted magnetic resonance spectroscopy

Genovese Guglielmo (1) (2), Santin Mathieu (1) (2), Palombo Marco (3), Valette Julien (4), Ligneul Clémence (4), Aigrot Marie-Stéphane (2), Felfli Mehdi (1), Abdoulkader Nasteho (1), Langui Dominique (5) (2), Millecamps Aymeric Millecamps (5) (2), Baron-Van Evercooren Anne (2), Stankoff Bruno (2), Lehéricy Stéphane (1) (2), Petiet Alexandra (1) (2), Branzoli Francesca (1) (2)

1. Center for NeuroImaging Research - CENIR [Paris], **2.** Institut du Cerveau et de la Moëlle Epinière = Brain and Spine Institute [Paris], **3.** Department of Computer Science and Centre for Medical Image Computing, University College of London (United Kingdom), **4.** Institut d'Imagerie Biomédicale, Molecular Imaging Research Center [Fontenay-Aux-Roses] (France), **6.** Plateforme d'Imagerie Cellulaire Pitié-Salpêtrière [Paris] (France)

20. Assessing tumor development with quantitative ultrasound and immunohistochemistry

Griffon Jérôme (1), Le Guillou-Buffello Delphine (1), Lamuraglia Michele (1), Bridal Lori (1)

1. Laboratoire d'Imagerie Biomédicale (LIB) [Paris] (France)

Quantitative Connectomic Histology

N Wang, PhD, RJ Anderson, PhD, A Badea, PhD, G Cofer, MS, Yi Qi, MD, GA Johnson, Ph.D
Duke Center for In Vivo Microscopy
Support: NIH 5P41EB015897, 1R01NS096720-01A1, K01 AG041211

The development of diffusion tensor imaging[1], tractography [2], and tract based structural connectomics has opened an extraordinary opportunity for exploration of neuroanatomy both clinically and in the basic sciences. We have become particularly excited about extending connectivity measurements from man to mouse (and rat). This talk will focus on the infrastructure, acquisition, reconstruction, post processing, and validation to make quantitative connectomic histology of the rodent brain routine and reliable.

Extension of methodologies from man to mouse is seldom straightforward. The problem(s) for connectivity measures are particularly daunting. A recent Nature Communications article[3] authored by 78 of the world's foremost experts in diffusion tractography concluded:

1) "To date, the approach (diffusion tensor tractography) has not been systematically validated in ground truth studies"
2) " ...most state of the art algorithms produce tractograms containing 90% of the ground truth bundles"
3) "**However, the same tractograms contain many more invalid than valid bundles …"**

Quantitative connectomics of the mouse brain must address the same issues encountered clinically at 3000 X higher spatial resolution. Our approach was to start with a foundation study; one that pushed the MR technology as far as possible in a fashion that would allow validation, the missing link in the clinical domain. That work [4] acquired 131 images (120 angular samples) of two perfusion fixed mouse brains using b values of 4000 s/mm^2. The total scan time for each specimen was 235 hours. We reasoned that a comprehensive data set was worth the effort even if it could only be done on a limited number of samples to understand what is possible with MR. That data was formatted so that it could be compared directly to the traditional fluorescent viral tracing studies, the gold standard performed by Oh et al [5] at the Allen Brain Atlas.

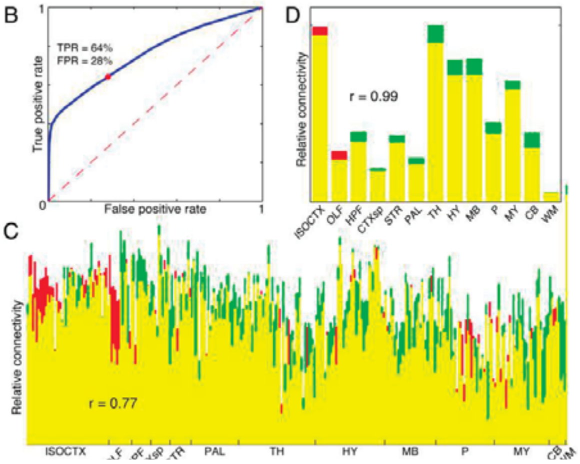

(**B**) ROC analysis of tractography accuracy with ABA tracer data as ground truth. (**C**) Mid-level (structure-level) comparison of tractography-based connectivity with tracer-based connectivity. Tractography-based connectivity estimates are shown in red, tracer-based estimates in green, and overlap between the two in yellow. (**D**) Coarse (parent-level) comparison similar to (**C**) but collapsed into ontologically defined parent structures. Parent structure abbreviations are consistent with the ABA. (from [4])

A ten day scan is not a viable long term protocol. We pursued two paths of acceleration. The first was a systematic study of the foundation set, down sampling the number of angular samples. The second employed compressed sensing, a method which under samples k-space and reconstructs the images using a nonlinear reconstruction algorithm [6].

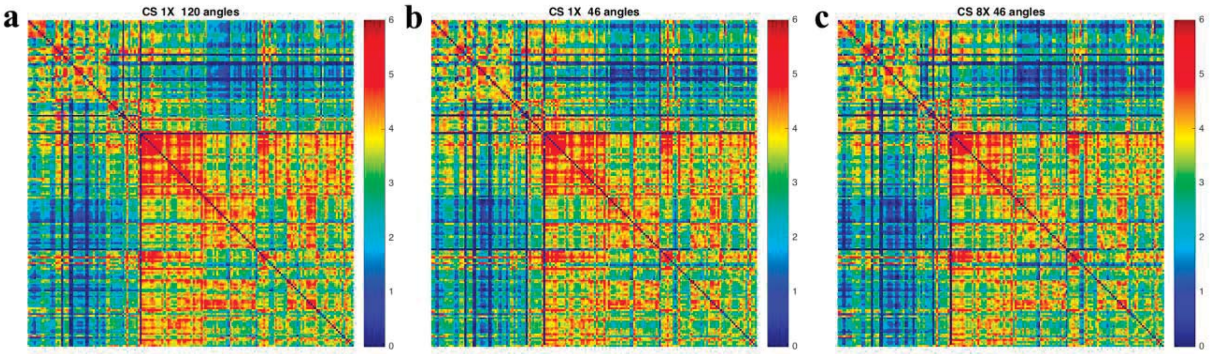

The connectome generated with a) 120 angles no k-space undersampling, b) 46 angles no k-space undersampling, and c) 46 angles with 8X k-space undersampling. The correlation coefficient between a) and b) is 0.9712, between a) and c) is 0.9695.

Conclusion

Our protocol acquires 46 angles plus 5 baseline images at 45 um resolution [7]. Data is streamed during acquisition to a high-performance cluster for iterative reconstruction [6]. The 3D volumes are registered to the baseline images and passed to a final pipeline that calculates diffusion tensor prameters, tractography, and the connectome. A single acquisition can be completed in 11 hrs allowing us to acquire two complete data sets per day. The data are not identical to that generated by retroviral tracers. But the agreement is far better than that suggested for clinical studies. We speculate that this arises from the fact that the voxels in our data are 10,000 X smaller than those in the clinical domain leaving a comparably smaller collection of fibers to resolve and reduced tracking errors. The resulting protocol is our best effort for a higher throughput method for reliable population studies of connectomics in the mouse brain.

References

1. Basser, P.J., J. Mattiello, and D. LeBihan, *MR diffusion tensor spectroscopy and imaging.* Biophys J, 1994. **66**(1): p. 259-67.
2. Hsu, E. and S. Mori, *Analytical expressions for the NMR apparent diffusion coefficients in an anisotropic system and a simplified method for determining fiber orientation.* Magnetic Resonance in Medicine, 1995. **34**: p. 194-200.
3. Maier-Hein, K.H., et al., *The challenge of mapping the human connectome based on diffusion tractography.* Nature Communications, 2017. **8**(1): p. 1349.
4. Calabrese, E., et al., *A diffusion MRI tractography connectome of the mouse brain and comparison with neuronal tracer data.* Cereb Cortex, 2015. **25**(11): p. 4628-4637.
5. Oh, S., Harris,JA,Ng,L, et al *A mesoscale connectome of the mouse brain.* Nature, 2014. **508**: p. 207.
6. Lustig, M., et al., *Compressed Sensing MRI.* IEEE Signal Processing Magazine, 2008. **25**(2): p. 72-82.
7. Wang, N., Anderson,RJ,Badea,A,Cofer,G, Dibb,R,Qi,Y,Johnson, GA, *Structural connectomics of the mouse brain using magnetic resonance histology.* NeuroImage, 2018. **Submitted**.

Multi-modality and multi-level data integration through brain atlasing: Human Brain Project tools and strategies

Jan G. BJAALIE

Institute of Basic Medical Sciences, University of Oslo, Norway

The Human Brain Project (HBP), an EU Flagship Initiative, is building an infrastructure that will allow integration of large amounts of heterogeneous neuroscience data. The ultimate goal is to develop a unified multi-level understanding of the brain and its diseases, and to emulate the computational capabilities of the brain. 3D reference atlases of the brain, including the Waxholm Space atlas of the rat brain and the Allen Mouse Brain Atlas, are key components in this infrastructure. The project develops new solutions for integrating and analyzing data and models in the context of the reference atlases. Users have access to FAIR (Findable, Accessible, Interoperable, and Re-usable) data and models through the HBP Knowledge Graph. A multi-step curation process serves to make data and models FAIR. The infrastructure is delivered by the HBP Neuroinformatics platform, in collaboration with the HBP High-Performance and Analytics Computing Platform based at the main supercomputer centers in Europe. New tools and workflows are now being developed to facilitate atlas based data integration and analysis.

Common Coordinate Frameworks in Animal Population Imaging

Mike HAWRYLYCZ, Ph.D.

Investigator, Director of Modeling, Analysis, and Theory, Allen Institute for Brain Science

Building on BRAIN Initiative-funded pilot studies begun in 2014, the BRAIN Initiative Cell Census Network (BICCN) is creating a comprehensive 3-D common reference mouse brain cell atlas that integrates molecular, anatomical, and physiological properties of brain cell types. Central to this effort is large scale cellular level profiling of the mouse brain including the development and extension of Common Coordinate Frameworks based on searchable digital atlases for data mapping, access, and navigation. The Allen Mouse Common Coordinate Framework (CCF) is an essential tool to understand the structure and function of the mouse brain at molecular, cellular, system and behavioral levels. It has been successfully used for large scale data mapping, quantification, presentation, and analysis and has evolved through the creation of multiple versions. Version 3 (v3) of the CCF is based on a 3D 10µm isotropic, highly detailed population average of 1675 specimens. Currently, CCF v3 consists of 185 newly drawn structures in 3D: 123 subcortical structures, 41 fiber tracts (plus ventricular systems), and 21 cortical regions including detailed primary visual and higher visual areas. A key to the BICCN effort is to refine and extend the 3-D Allen Institute CCF for the mouse to enable external mapping of key single cell modalities in a 2D and 3D anatomic context for access and visualization at cell, and nuclei level. We survey these use cases and approaches and discuss image based mapping and navigation tools for cell location, context and ontology.

The Boon and Bane of Animal Population Imaging - A Pharma Industry's Perspective

Basil KUENNECKE

Translational Technologies for Neuroscience, Ophthalmology and Rare Diseases
Roche Pharma Research and Early Development, Roche Innovation Center Basel
F. Hoffmann-La Roche Ltd, CH-4070 Basel, Switzerland

Introduction

Population studies with large sample sizes are scientifically enticing because of their promise to help elucidate complex medical conditions that root in numerous minor, yet cumulative genetic liabilities and environmental influences. In many of these studies, imaging plays a pivotal role as a rich source of biomarkers for deep phenotyping. Whilst in the clinical realm this concept has been thriving, animal population imaging is still in its infancy for reasons that are manifold.

Imaging readouts have become essential tools for decision taking in the drug discovery process. Magnetic resonance imaging (MRI) is particularly valued and extensively used for benchmarking and differentiation of novel drug candidates and evaluation of translational imaging biomarkers in later stages of in vivo testing, for initial proof-of-concept studies, and for characterisation of new animal models. In these settings, reliability, long-term stability and relevance of the readouts are of utmost importance and thus are bolstered with extensive method qualification. Pharmacological studies are generally performed in specific and well-defined animal models whose genetic backgrounds and environmental influences are painstakingly monitored to reduce variability and drifts as much as possible. Notably, animal population imaging akin to human population imaging is rarely, if at all, found in drug discovery. However, collections of many smaller-sized and focused studies are often at hand and may serve as a basis for what we dub "composite" animal population imaging. Here, we give a pharma industry's perspective with focus on the contribution of MRI.

Methods

All animal studies reported herein were carried out with the ethical approval and according to the regulations of the Swiss Federal Food Safety and Veterinary Office. Data were acquired with a Bruker BioSpec 4.7T / 40cm or BioSpec 9.4T / 20cm MRI scanner. Composite population analyses encompass data of hundreds to several thousands of subjects accrued from studies carried out over several years.

Results and Discussion

One of the opportunities arising from composite animal population imaging is the appraisal and comparison of animal models for complex disorders with the aim to elucidate a potential common underlying biological disease substrate. The challenges faced in this domain are best explained at the example of investigations carried out in a selection of etiologically diverse animal models for autism spectrum disorder (ASD)[1,2]. Such population studies are large-scale undertakings considering the number of models, group sizes and study repeats required for statistical validation that would call for a distributed approach such as a consortium effort. Cross-institutional dissemination of digital data acquisition and processing procedures is of a lesser concern today and a protocol standardisation at this level can be achieved with limited effort. "Soft" factors related to animal handling, housing, timing, etc. however are difficult to capture and their influences are often underestimated and thus constitute major sources of unaccounted experimental variability. As an alternative, researchers have resorted to multiple-animal imaging set-ups to increase the throughput of a single site by simultaneously acquiring data from several animals with one MRI scanner[3]. Whereas this parallel approach has been successfully applied to MRI morphometry, limitations are manifold for neurometabolic and neurofunctional readouts that require an accurate and constant timing for all subjects. For large-scale body composition analyses in the field of metabolic disorders we have resorted to yet another innovative approach. Spatial resolution, i.e. imaging, is traded in for the speed and physico-chemical selectivity of a whole-body relaxometric assessment of fat and lean mass. Notably, this modality doesn't require anaesthesia and affords the least interference with the animals' physiology, thus providing highly accurate and pharmacologically relevant data at a throughput of 30 animals per hour[4].

Composite animal population imaging on control or vehicle treated subjects is a great resource of data for long-term quality assurance with regard to stability and reproducibility of readouts and the underlying experimental procedures. MRI quality parameters such as signal-to-noise and contrast-to-noise as well as main readouts are expected to remain stable over time on the premise that standardisation with standard operation procedures (SOPs) is in place and homogeneous animal populations are being used. Under these conditions, already small deviations that would remain unnoticed at the single animal or group level become apparent, even though in retrospect only. We have recently reported an unexpected finding obtained by perfusion-based functional MRI in Fischer 344 rats, i.e. an inbred line widely used as a model of high trait anxiety for testing drug efficacy. Under such seemingly highly standardised conditions the population separates into two distinct phenotypes with high and moderate basal neural activity in the medial prefrontal cortex, respectively[5]. Although the underlying cause has remained elusive the data suggest that anxiety-related circuitries are involved.

A third, very powerful application of composite animal population imaging is found in pharmacology. On the premise that stable conditions and readouts are maintained over many studies and extended periods of time as outlined before, drug treatment with different compounds and dose levels can be introduced as the driving variable. We have pioneered this approached in the field of pharmacological MRI (phMRI) of psychotropic compounds. Multivariate statistics on these data have revealed neural activity maps and key features of circuitry engagement for different drug classes and modes-of-action. Composite measures of the feature space, so-called gauges, have been established for antipsychotics, anxiolytics and antidepressants that now serve as a reference framework for benchmarking, positioning and differentiation of novel compounds with advanced pharmacology[6].

Conclusions

To date, genuine animal population studies are scant as a consequence of the massive resourcing that would be required. High standardisation as imposed in the pharma discovery environment is, however, a propitious foundation for composite animal population imaging which is based on data garnered from collections of individual studies. Such population studies have provided unprecedented insight into subtle and complex biological processes and thus have informed and spurred the subsequent discovery efforts.

References

1. Petrinovic MM, et al. Proc Intl Soc Magn Reson Med 2014; 22:2099.
2. Horder J, et al. Translational Psychiatry 2018 (in press).
3. Dazai J, et al. J Vis Exp 2011; 48:e2497.
4. Künnecke B, et al. Obes Res 2004; 12:1604-1615.
5. Bruns A, et al. Proc Intl Soc Magn Reson Med 2018; 26 (in press)
6. Bruns A, et al. Neuroimage 2015; 112:70-85.

Automating image processing with machine learning

Anna KRESHUK

Heidelberg University / EMBL

Machine learning is advancing the state-of-the-art in computer vision more rapidly than ever before: for many problems in natural image processing automated methods are now approaching human parity. One of the major advantages of learning-based approaches is their general applicability: tailoring to a particular problem is performed by providing suitable training data, while the core of the algorithm remains unchanged. The results obtained by such a generic approach are often sufficiently good to only require minimal manual correction. I will address the problem of image segmentation and show, on examples from the nanoscale connectomics domain, how an image processing pipeline can be bootstrapped from sparse interactively provided user annotations to process Terabytes of volumetric image data.

SBA Composer: web-based software for exploring brain slices, volumes and surfaces in a 3d atlasing context

Rembrandt BAKKER[1,2], Anastasia OSOIANU[1], Martin ØVSTHUS[3], Trygve B. LEERGAARD[3], Paul TIESINGA[1]

1. Neuroinformatics department, Radboud University, Nijmegen, the Netherlands.
2. Institute of Neuroscience and Medicine (INM-6), (IAS-6) and (JBI-1 /INM-10), Jülich Research Centre, Jülich, Germany.
3. Department of Anatomy, Institute of Basic Medical Sciences, University of Oslo, Norway.

Fully automated analysis pipelines are important when vast quantities of data need to be processed. In such pipelines quality control is typically based on visual inspection by a human operator. We here present *SBA Composer*, a web-based tool optimized for visual inspection of image registration results and exploration of slice-based, volumetric and surface-based data in a 3d atlasing context. The tool, available from https://scalablebrainatlas.incf.org/composer, is an extension of the Scalable Brain Atlas [1], which provides web-based access to 30 brain atlases (MRI and parcellations) of 7 different species. SBA Composer is at an early stage of development, and we here demonstrate its stable features on the basis of two use case examples.

Use case 1: Aligning Macaque Nissl sections

This use case takes coronal Nissl sections from the NIH Blueprint Non-Human Primate atlas [http://www.blueprintnhpatlas.org/], aligns the individual images to an MRI of the same individual, and co-registers the result to the Macaque atlas of Calabrese et al. [3]. The pipeline uses the POSSUM toolbox of Majka et al. [4] to carry out three steps: (1) pair-wise sequential alignment, (2) coarse-to-fine registration, and (3) deformable registration.

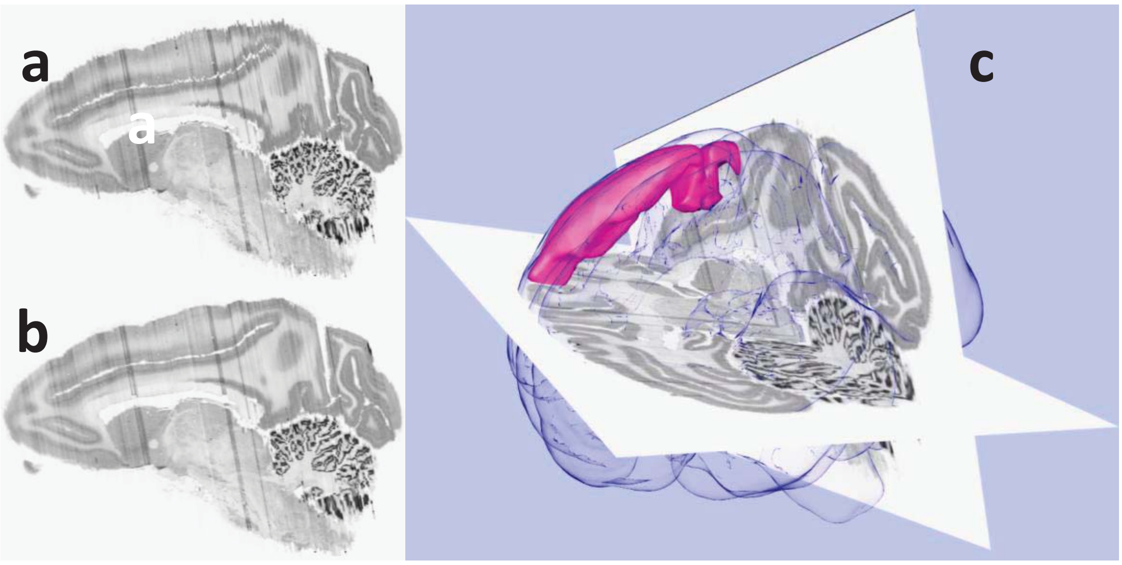

Figure 1: *Aligned NHP Nissl sections: (a) before deformable deformation, (b) final result, and (c) volume cuts at arbitrary angles, with brain silhouette (blue) and primary motor area (purple).*

Currently, SBA Composer supports the following file formats: 3d objects (X3D - xml-based 3d graphics), 2d images (JPEG, PNG, TIFF), data volumes (Nifti-1, ITK MetaImage, Freesurfer MGH/MGZ, NRRD Raw Raster Data), slice stacks (QuickNii, use case 2). It uses the x3dom library [2] as the graphics engine, with custom shaders for displaying volume cuts and overlays. Data processing is done on the client, the size of images that can be loaded depends on the client's memory and GPU. Consequently, SBA Composer has very modest server requirements.

Use case 2: Verifying the alignment of In Situ Hybridization image sections

Coronal sections from *in situ* hybridization experiments in mouse were obtained from the Allen Brain Atlas data portal [http://www.brain-map.org/; 5] and re-aligned using QuickNii [6]. A QuickNii file reader was added to SBA Composer, which can be used to fine-tune the alignment. It has display modes (checkerboard, transparency) for overlaying slices with volumetric data. Imaging modalities from the atlas can be sliced at arbitrary angles. Voxel interpolation is done on the client GPU.

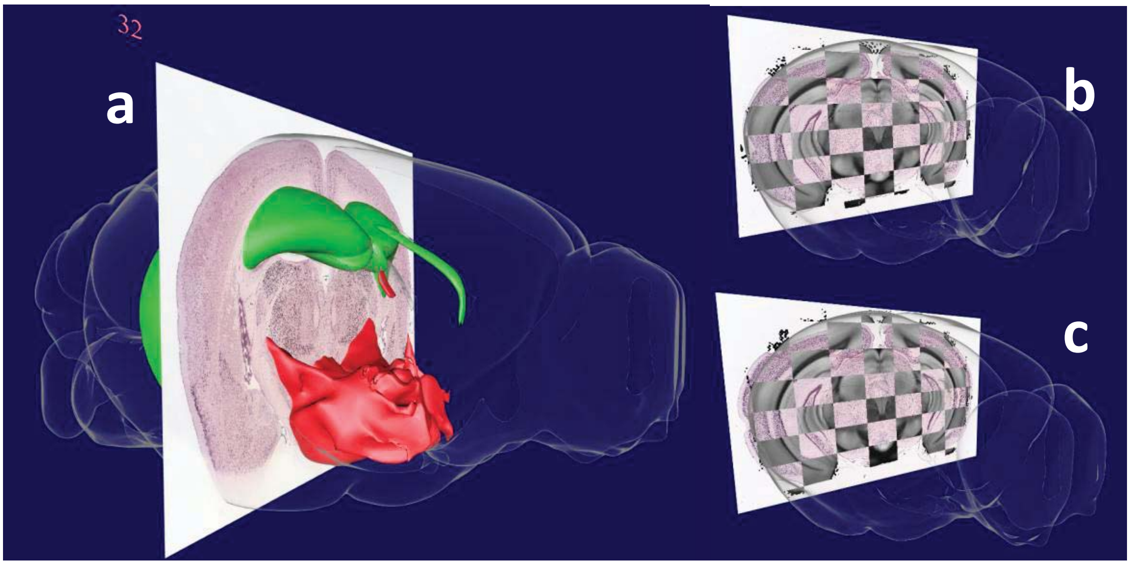

Figure 2: *ISH image, aligned with QuickNii, with (a) hippocampus (green) and hypothalamus (red), (b) checkerboard overlay with T1-like data, and (c) original Allen Institute automated alignment.*

Future development of SBA Composer includes (1) document format to save the state of the viewer and share it online; (2) integration with the HBP Morphology Viewer [7], to display neuronal reconstructions created in Neurolucida [MicroBrightField Inc.], and (3) integration with the Microdraw service [http://microdraw.pasteur.fr] to annotate datasets at microscopic resolution.

References

1. Bakker R, Tiesinga P, Kötter R. The Scalable Brain Atlas: Instant Web-Based Access to Public Brain Atlases and Related Content. Neuroinformatics. 2015;13(3):353-366. doi:10.1007/s12021-014-9258-x.
2. Arbelaiz A, Moreno A, Kabongo L, and García-Alonso A. X3DOM volume rendering component for web content developers. Multimedia Tools Appl. 2017;76(11):13425-13454. doi:10.1007/s11042-016-3743-1.
3. Calabrese E, Badea A, Coe CL, et al. A diffusion tensor MRI atlas of the postmortem rhesus macaque brain. NeuroImage. 2015;117:408-416. doi:10.1016/j.neuroimage.2015.05.072.
4. Majka P, Wójcik DK. Possum—A Framework for Three-Dimensional Reconstruction of Brain Images from Serial Sections. Neuroinformatics. 2016;14:265-278. doi:10.1007/s12021-015-9286-1.
5. Sunkin SM, Ng L, Lau C, et al. Allen Brain Atlas: an integrated spatio-temporal portal for exploring the central nervous system. Nucleic Acids Research. 2013;41:D996-D1008. doi:10.1093/nar/gks1042.
6. Puchades M, Csucs G, Checinska M, Øvsthus M, Bjerke IE, Andersson K, Leergaard TB, Bjaalie JG, Program No 532.12, 2017 Neuroscience Meeting Planner. Washington, DC: Society for Neuroscience; 2017.
7. Bakker R, Tiesinga P. HBP neuron morphology viewer [version 1; not peer reviewed]. F1000Research 2016, 5:2282 (poster). doi:10.7490/f1000research.1113110.1.

Supported by the Human Brain Project through the European Unions Horizon 2020 Programme under Grant Agreement No. 720270 (HBP SGA1), and Flag-ERA project FIIND ‘Ferret Interactive Integrated Neurodevelopment Atlas’, grant no. NWO 054-15-104.

The electronic collection of vertebrate brains of the National Natural History Museum of Paris

Katja HEUER[1,2], Melanie DIDIER[3,4], Antoine BURGOS[3,4], Stephanie ANASTACIO[3,4], Marc HERBIN*[5,6], Mathieu SANTIN*[3,4] and Roberto TORO*[1,3]

[1]Institut Pasteur
[2]Max Planck Institute
[3]Sorbonne Universités, UPMC Univ Paris 06, CNRS, INSERM, APHP GH Pitié-Salpêtrière, Institut du cerveau et de la moelle épinière (ICM), F-75013 Paris, France
[4]Centre de Neuro-Imagerie de Recherche (CENIR), Paris, France
[5]National Natural History Museum of Paris
[6]CNRS
*Authors contributed equally to this work.

Introduction

Understanding the evolution of the brain across species should allow us to better understand the sources of the normal and pathological variability in the human brain – a major challenge for neurosciences today. An analysis of neuroanatomical evolution and conservation should not only allow us to detect the traces of evolution in different brain systems and regions, it should also allow us to evaluate the degree of phenotypic conservation across species, providing a framework to better understand natural variability, and to distinguish it from pathological variability.

We have begun to constitute an open-access collection of high quality vertebrate brain MRI. We are currently scanning and processing the Vertebrate Brain Collection of the National Museum of Natural History, Paris, France. To date, more than 200 brains from different species have been scanned and will soon be made publicly available. Over the next five years, this digital collection should grow to > 1900 different specimen.

Methods & data

The specimens come from the collection of vertebrates of the National Museum of Natural History (MNHN) Paris – one of the oldest and largest collections of vertebrate brains in the world. This unique resource comprises almost 2,000 extracted brains and more than 10,000 full specimens, ranging from lissencephalic small brains such as that of a tortue imbriquée to the large and tremendously folded brain of a Bottlenose dolphin.

High resolution MRI images have been acquired at the Center for Neuroimaging Research (CENIR) of the Institut du Cerveau et de la Moëlle Épinière (ICM, Paris, France) using either a 3T Siemens Tim Trio system, a Siemens Prisma or an 11.7T Bruker Biospec. Each dataset was acquired with a 3D gradient-echo sequence (FLASH). Parameters (Field of View, Matrix size, TR, TE) were adjusted so as to obtain the highest resolution possible with our scanner (from 100 to 450 μm isotropic). TR and TE were always chosen as minimum. Flip angle was fixed to 20° at 3T and 10° at 11.7T. The number of averages was chosen to maintain a scanning time below 12 hours.

Results

Our first data release provides access to more than 30 brains, including in particular the brain of a Thylacine – a marsupial extinct in the early 20th century. As an example, the figure shows a Sloth bear brain, a leopard, a platypus and a thylacine brain and the 3D surface reconstructions.

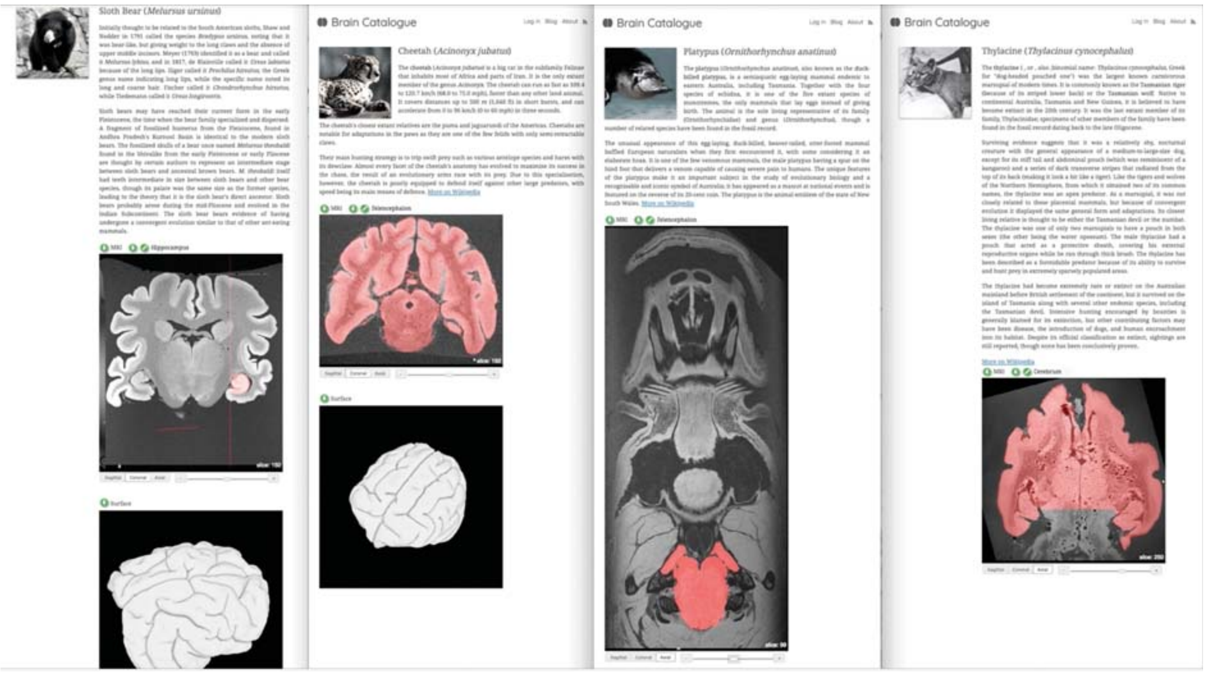

We created a special framework to present and share the data: The Brain Catalogue — a Web-based, interactive, virtual museum of the vertebrate brain and a platform for the collaborative study of brain anatomy (available at https://braincatalogue.org). The Brain Catalogue allows everyone to browse through high resolution MRI slices, explore available 3D cortical reconstructions and learn about the diversity of vertebrate brains. The Brain Catalogue is at the same time a tool where citizen scientist can join and contribute to the segmentation of brains in our collection.

Conclusion

This is the first publicly available dataset which spans such a large variety of brains of different species. Our Web platform, the Brain Catalogue, should foster the reutilisation of the data by the research community as well as by citizen scientists.

Towards a connectome atlas of the C57Bl6 mouse brain using ex vivo ultra-high field diffusion MRI

Ivy Uszynski[1,2], Hervé Mathieu[1,2,3,4], Jean-Christophe Deloulme[1,2], Emmanuel L. Barbier[1,2], and Cyril Poupon[5]
[1]GIN, Université Grenoble Alpes, Grenoble, France, [2]INSERM U1216, Grenoble, France, [3]Unité Mixte de Service IRMaGe, Grenoble Alpes Hospital, Grenoble, France, [4]Unité Mixte de Service 3552, CNRS, Grenoble, France, [5]NeuroSpin, CEA Saclay, Gif-sur-Yvette, France

Purpose: Diffusion MRI (dMRI) is a powerful tool to investigate the structural connectivity of the brain and to characterize its microstructure. Ultra-high field preclinical MRI systems are equipped with very strong gradients that allow to reach a much higher spatial and angular resolution in animal models, thus offering the possibility to segment white matter bundles in a similar way to what was achieved previously in humans. In this study, we propose to adapt the massive clustering approach of Guevara [1] to rodents in order to establish the foundations of a novel atlas of the structural connectivity of C57Bl6 mice brains that will be validated against a histological ground truth. To this aim, 3D High Angular Resolution Diffusion Imaging (HARDI) was performed ex vivo on C57Bl6 mice brains and clusters of fibers were eventually computed using an automated procedure.

Material and methods:

Acquisition Protocol - Experiments were performed on a 9.4T horizontal scanner (Bruker Biospec, AVIII-HD, Grenoble MRI facility IRMaGE) with a volume coil for excitation (86 mm inner diameter) and a 4-channel cryoprobe surface coil for reception. A 3D diffusion-weighted Pulsed Gradient Spin Echo echoplanar (EPI) sequence was implemented with the following parameters: 8-shots, TR/TE=640/26.0ms, diffusion gradients characteristics δ/Δ = 3.6/9.4 ms, 60 diffusion directions with a b-value of 3000 s/mm² and 6 b=0s/mm² reference images, isotropic resolution of 100 µm, 2 averages, total acquisition time of 18h. The computation of an active second order shim (performed on an ellipsoidal shim volume within the mouse brain) was performed beforehand to correct for magnetic field inhomogeneity. A 40-minutes long 3D T2-weighted TurboRARE acquisition with the same field of view and resolution as the diffusion sequence was eventually performed for anatomical landmarks and registration purposes.

Animals - The MRI protocol was applied to twelve ex vivo C57Bl6 mice (6 females, 6 males, 9 – 11 weeks old). Following intracardiac perfusion (4% paraformaldehyde + Gd-DOTA), the animal was decapitated and the fixed head was imaged.

Post-processing - The analysis of the data was performed using the Connectomist toolbox[2]. After correction for sources of artifacts (outliers, eddy currents, motion), an affine registration of the DW dataset to the anatomical T2-weighted image using a mutual information similarity measure was performed. Orientation distribution functions (ODFs) were then computed using the analytical Q-ball model[3] (spherical harmonics order 6, regularization factor 0.006). A deterministic regularized streamline tractography[4] was performed to infer a dense whole brain connectogram per animal (~3.200.000 connections) using the following parameters: uniform seeding over a predefined domain of propagation computed from the average b=0s/mm² reference image (8 seeds per voxel), forward step of 20 µm, aperture angle of 30°.

Two approaches were then led to analyze the data:

i. A connectivity matrix approach, based on the computation of the number of fibers connecting a pair of anatomical regions. For this step, we used a C57Bl6 mouse brain atlas inspired from (Calabrese et al. 2015)[6] composed of 267 cortical as well as subcortical regions. A non-linear 3D registration procedure using ANTs software[5] was used to register the T2-weighted scan to the atlas using a diffeormorphic registration based on Symmetric Normalization (SyN)[7] with a mutual information similarity measure. Fig. 3 represents the average as well as standard deviation connectivity matrices (dimensions: 267x267) on the twelve mice population – each point representing the number of fibers connecting a pair of regions (roi_i, roi_j) of the atlas.
ii. An intra-subject fiber clustering approach. This method consists in the automatic clustering of individual tractography fibers into fiber bundles for each mouse, without using a mouse brain atlas. After dividing the fibers into 10 length groups (0-3/3-6/6-9/9-12/12-15/15-18/18-21/21-24/24-27/27-30 mm, fiber resampling step=0.01), a 100 µm resolution parcellation volume based on a K-Means algorithm was calculated for each range length (minimum parcel size of 27 voxels). A hierarchical clustering procedure based on the computation of a connectivity matrix between these parcels was then performed for each range length to retrieve clusters of parcels (minimum cluster size of 300 voxels, average cluster size of 3000 voxels, connectivity matrix threshold of 1%). All fibers intersecting one same cluster by more than 60% of their length were assigned to the same resulting bundle, leading to the final white matter bundles for each mouse. Eventually, the centroid of each bundle was computed using the mean fiber approach (Fig.4).

Results: The diffusion data (Fig. 1) underwent deterministic regularized streamline tractography. Fig. 2a allows for a better understanding of the complex whole-brain white matter tractogram of Fig. 2b, with the characterization of the different fiber length computed. Fibers from 6 to 9 mm long represent the largest group in a C57Bl6 mouse brain. Measuring connectivity matrices also permits to disentangle the data by emphasizing the main pathways within the brain (Fig 3b). As expected, the corpus callosum (label 219) is strongly linked with the regions composing the cerebral cortex with a 65% standard deviation. Other regions show a much higher standard deviation, as for instance the cingulum region (labels 223-224). This can be related to its relatively small size: the cingulum represents less than 0.1% of the atlas volume. Fig. 4 represents the centroids of the fiber bundles (mean fiber bundles) after computation of intra-subject fiber clustering for 3 typical mice. Each centroid represents in average 130 fibers regrouped in a bundle.

Discussion: In this study, we show the successful measurement of ex vivo high-resolution whole-brain 3D diffusion in twelve C57Bl6 mice. The complexity of the atlas – with numerous small size regions (only 26 regions out of 267 represent over half the volume of the atlas) – requires a perfect matching on the diffusion dataset to preserve a low standard deviation. The main perspective of this project is to compute inter-subject fiber clustering that will allow us to build the C57Bl6 mouse connectivity atlas itself.

Acknowledgements Grenoble MRI facility IRMaGe was partly funded by the French program “Investissement d’Avenir” run by the ‘Agence Nationale pour la Recherche’ ; grant 'Infrastructure d’avenir en Biologie Santé' – ANR-11-INBS-0006

References: 1. Guevara, P. et al., 2011. Robust clustering of massive tractography datasets. *NeuroImage*.
2. Duclap, D. et al., 2012. Connectomist-2.0: a novel diffusion analysis toolbox for BrainVISA. In *29th ESMRMB*. Lisbone, Portugal
3. Descoteaux, M. et al., 2007. Regularized, fast, and robust analytical Q-ball imaging. *Magnetic Resonance in Medicine*
4. Perrin, M. et al., 2005. Fiber tracking in q-ball fields using regularized particle trajectories. *Proceedings of the Information Processing in Medical Imaging conference*
5. Avants, B.B. et al., 2012. A Reproducible Evaluation of ANTs Similarity Metric Performance in Brain Image Registration. *NeuroImage*
6. Calabrese, E. et al., 2015. A Diffusion MRI tractography connectome of the mouse brain and comparison with neuronal tracer data. *Cerebral Cortex*
7. Avants, B.B. et al., 2008. Symmetric diffeomorphic image registration with cross-correlation: Evaluating automated labeling of elderly and neurodegenerative brain. *Medical Image Analysis*

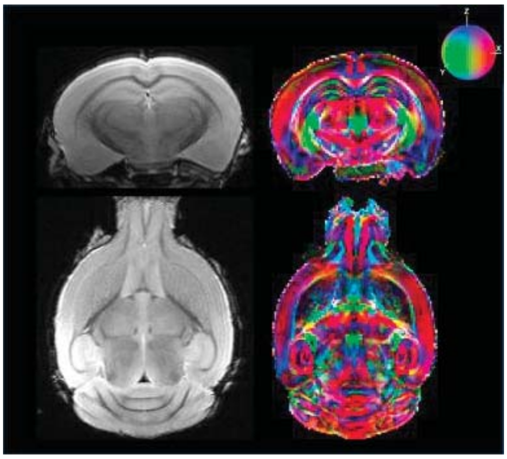

Fig. 1: Anatomical T2-weighted axial and coronal views and corresponding color-coded FA maps for one C57Bl6 mouse.

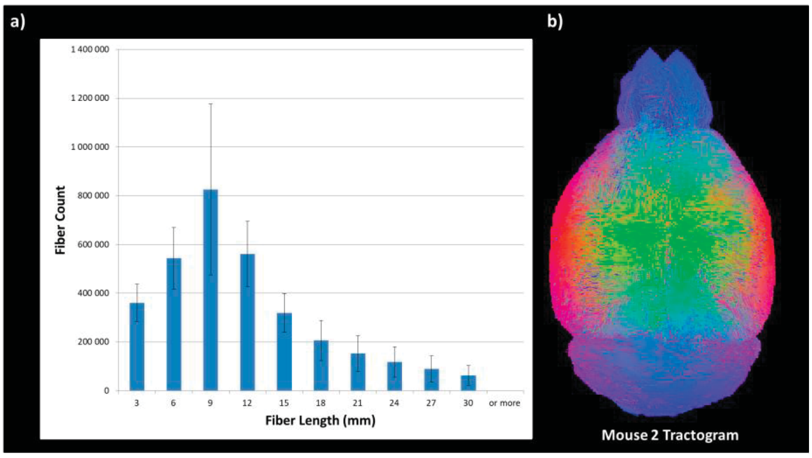

Fig. 2: (a) Average of the number of fibers found in each length interval (0-3/3-6/6-9/9-12/12-15/15-18/18-21/21-24/24-27/27-30 mm or more) for the twelve mice after deterministic regularized tractography (Mean ± SD). (b) Whole tractogram for one C57Bl6 mouse (~ 3.2x10^6 fibers). On this figure, color is not related to fiber direction and is used for visualization purposes.

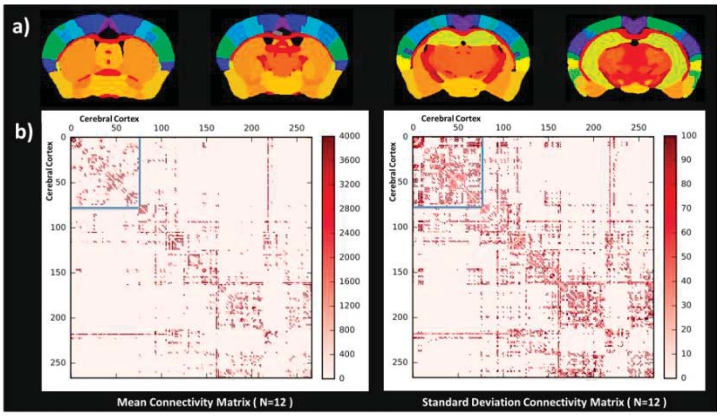

Fig. 3 : (a) Selection of four axial slices of the mouse brain atlas composed of 267 regions. (b) Mean (left) and standard deviation (expressed in percentage of the mean) (right) connectivity matrices for twelve C57Bl6 mice. Each point of the matrices represents the number of fibers connecting two regions. The up-left corner – blue box – represents the regions of the cerebral cortex. Label 219 and 223-224 respectively represent the corpus callosum and the cingulum (right and left parts).

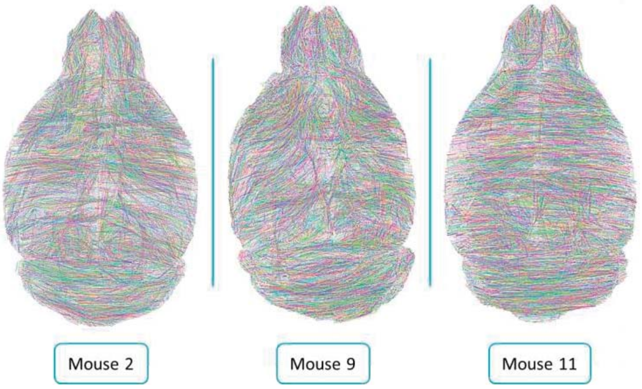

Fig. 4: Comparison of intra-subject fiber clustering results for three mice from a sagittal point of view. On this figure, color is representative of a specific bundle.

Surface-based cortical parcellation and atlas creation of the sheep brain

Scott LOVE, Marine SIWIASZCZYK, Christophe DESTRIEUX, Frederic ANDERSSON, Elodie CHAILLOU

[1]PRC, INRA, CNRS, IFCE, Université de Tours, Nouzilly, France.
[2]UMR 1253, iBrain, Université de Tours, Inserm, Tours, France.

The sheep model is a compelling yet underused model for understanding structure and function of the cortex. Neuroanatomical labelling facilitates the generalizability and comparability of experimental results across studies and laboratories. While brain-labelling atlases have largely focused on subcortical regions in sheep, very little information is available about the cortical parcellation. The current work aimed to use modified Freesurfer pipelines to produce a surface-based labelling of the sheep cortex, facilitating neuroimaging investigations of this large-animal model.

The probabilistic surface-based labelling will be formed from high-resolution (0.6 mm^3) T1-weighted MR images collected using a 3T Siemens Magnetom Verio. Twenty two-year old Ile de France ewes from the Experimental unit UEPAO-INRA (Nouzilly, France) were anesthetized and subjected to *in vivo* MRI imaging. The experiment was conducted at the platform CIRE in accord with French legislation and guidelines on experimental animal care.

A multi-atlas skull stripping procedure was created and used to remove non-brain tissue from the T1w images. Subcortical regions were then manually segmented and removed from the skull stripped images before using the Freesurfer software to produce cortical surface reconstructions. Major sulci and gyri were manually delineated on the inflated version of the cortical surface, which exposes the otherwise hidden sulci. Each region was assigned a colour and corresponding label in accord with nomenclature based on literature and veterinary terminology.

This project was performed with financial support from CIPhase, Inra and Region Centre (NeuroGéo) and with the help of Hans Adriaensen, Frédéric Elleboudt, Gilles Gomot, Christian Moussu and Luc Perrigouard from the platform CIRE.

Construction of an MRI-Based Connectome for the Marmoset Brain: Methods and Initial Results

Cecil Chern-Chyi YEN, Cirong LIU, Diego SCZUPAK, Madeline MARCELLE, Afonso SILVA

National Institutes of Health

Introduction

The human connectome project (HCP) is the most successful multi-center collaboration efforts aimed at mapping neural connections of the human brain[1]. The success of the HCP may be attributed to having standardized MRI protocols that are optimized for instruments of various centers. A pilot version of the HCP-style protocol has been developed for 7T[2]. Ultra-high field MRI provides unprecedented spatial resolution and sensitivity, which can be combined to facilitate detection of finer and hidden brain connections. These brain networks obtained from healthy subjects build a solid baseline for comparative studies of patients with either acquired or congenital brain disorders. However, to investigate the etiology and treatments of such disorders, an animal model whose brain networks and gnome share a high degree of similarity to humans is desired. The common marmoset, a small New World primate, has shown to pose these two properties. In addition, germline transgenesis in marmosets opens the opportunity to create a non-human primate model of many congenital brain disorders[3]. Despite the enormous potential of the marmoset model, a population-averaged baseline of marmoset's brain connections is still lacking. Our group is one of the pioneers in resting-state functional MRI (rfMRI) of awake marmosets[4]. The use of awake marmosets in functional imaging studies eliminate the confounds of general anesthesia, that hampers the detectability and interpretation of brain networks and increases data variability across multi-centers. Therefore, the aim of this study is to create a standardized MRI protocol for constructing the marmoset connectome, that will hopefully promote interinstitutional collaborations.

Material and Methods

All procedures were approved by the ACUC of the NINDS. Seven adult male marmosets (age: 2-7 years old) were acclimated to the body and head restraint inside a horizontal 7T/30cm MRI spectrometer (Bruker., Billerica, USA). Marmosets were laid in the sphinx position in the cradle, and their heads were comfortably immobilized by individualized 3D-printed helmet and chin-piece[5]. Under sphinx position, marmoset's body would be lower than its head and would not fit into 9cm volume transmission coil normally came with 12cm gradient coil. Thus, a 15cm gradient coil (RRI., Billerica, USA) was used with an 11cm custom-built birdcage coil. A custom-built 10-element phased array RF coil was placed on top of the helmet. FLASH and RARE sequence was used to align three-orthogonal planes to the mid-sagittal plane and the line connecting anterior and posterior commissure. Anatomical MRI data was acquired using a RARE sequence from 38 coronal slices with 0.5 mm isotropic resolution. A pair of spin-echo EPI with opposite phase-encoding gradient were acquired for correction of the susceptibility-induced off-resonance field. rfMRI data were acquired using a single-shot gradient-echo EPI sequence. Four to six rfMRI scans with 512 repetitions were performed in each session. MRI protocols and parameters can been found in figure 1. Pre- and post-processing of the data were done using AFNI, FSL and ANTS, which can be incorporated into an unattended batch script and register to NIH's marmoset brain atlas[6].

Results

Study-specific anatomical MRI images show excellent image quality and tissue contrast. The slice thickness and number were deliberately kept the same as the rfMRI for easier importing geometry. The co-planar rfMRI images achieve good SNR (>20 for all images) and temporal stability. EPI distortion due to the susceptibility-induced off-resonance field was minimized using a pair of blip -up and -down EPI and FSL's topup. Three major hubs (dlPFC, PCC, and PCRSC) of default mode network are observed in all seven marmosets (figure 2).

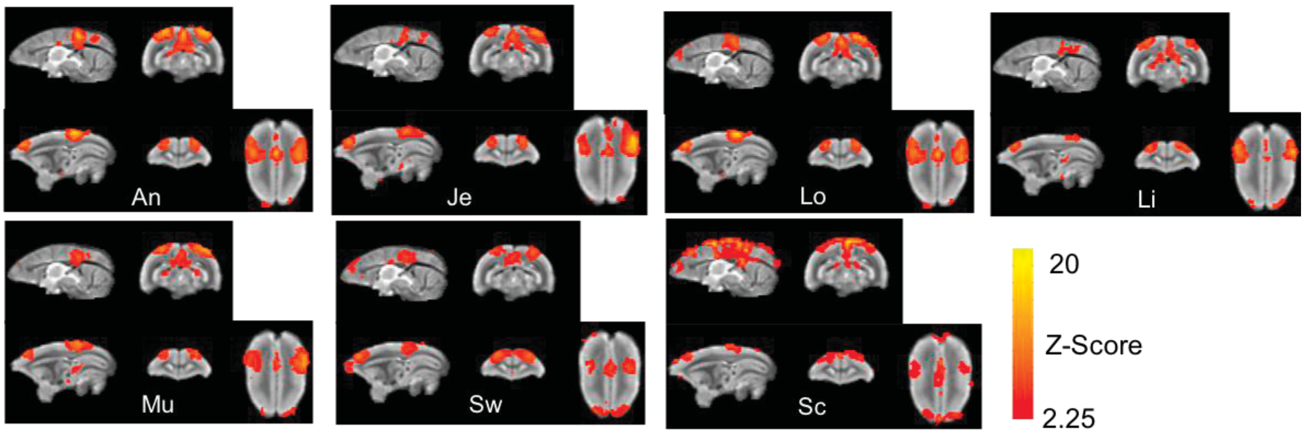

Discussion/Conclusion

Our MRI protocol and processing pipeline of marmoset connectome follow the well-considered HCP-style MRI protocol of 7T and its processing pipeline. Due to the difference in marmoset vs. human brain and pre-clinical vs. clinical MRI, exceptions and limitations are inevitable. First, the spatial resolution was determined to be 0.5mm isotropic, which was the best resolution achievable with acceptable SNR. Second, we chose the longest axis (anterior-posterior) as our frequency-encoding direction and left-right axis as our phase-encoding direction for parallel imaging. The slice-selection direction is along the shorter dorsal-ventral axis and hence limits multiband capability. Third, our TR is set to 2s due to the limitation of the gradient duty cycle without multiband acceleration. In conclusion, we developed an MRI protocol for imaging awake marmosets following the methodology of the HCP. Our MRI protocol and process pipeline can be easily adopted across centers currently interested in imaging the marmoset brain. We believe our standardized MRI protocol will encourage the development of global collaborations, and lead to a further utilization of the marmoset model in translational neuroscience studies.

References

1. Van Essen, D.C., et al., *The WU-Minn Human Connectome Project: an overview.* Neuroimage, 2013. **80**: p. 62-79.
2. *HCP Protocols*. 2014; Available from: http://protocols.humanconnectome.org/.
3. Park, J.E., et al., *Generation of transgenic marmosets expressing genetically encoded calcium indicators.* Sci Rep, 2016. **6**: p. 34931.
4. Belcher, A.M., et al., *Large-scale brain networks in the awake, truly resting marmoset monkey.* J Neurosci, 2013. **33**(42): p. 16796-804.
5. Papoti, D., et al., *An embedded four-channel receive-only RF coil array for fMRI experiments of the somatosensory pathway in conscious awake marmosets.* NMR Biomed, 2013. **26**(11): p. 1395-402.
6. Liu, C., et al., *A digital 3D atlas of the marmoset brain based on multi-modal MRI.* Under revision, 2017.

Sharing research imaging data in « Imageries du Vivant ». An ongoing experience at Sorbonne Paris Cité University (SPC).

L. Abidi[1] , P. Garteiser[1,a] , C. Cerin[1,b] , M. Smadja[2] , S. Sahri[1c] M. Bentounsi[1,d] D. Geldwerth[1e], S. Li-Thiao-Té[1e], Y.-M. Frapart[1,f]

1 Sorbonne Paris cité University, Paris
a INSERM- University Paris Diderot b LIPN, Paris Nord University
c LIPADE, Paris Descartes University e LAGA UMR CNRS- Paris Nord University
f UMR 8601 CNRS- Paris Descartes University
2. SisNcom

Since 2008, Paris Descartes, Paris Diderot and Paris Nord universities are building-up an interdisciplinary network called « imageries du Vivant ».around multiscale, multimodality interdisciplinary imaging research

This network focuses on three main efforts :

- **Atlas IDV**: A multiscale, multimodality interdisciplinary Linked Open Data sharing project composed of different tools developed for sharing data, algorithms and software elements, creating an image data base, with visualization, processing and crowdsourcing possibilities.
- **New Imaging biomarker** emergence and validation, coming from new modalities, new contrast agents and/or methodological developments.
- **Societal and ethical** implications of imaging.

This network is composed of more than 30 research teams or facilities from Sorbonne Paris Cité University distributed in Paris.

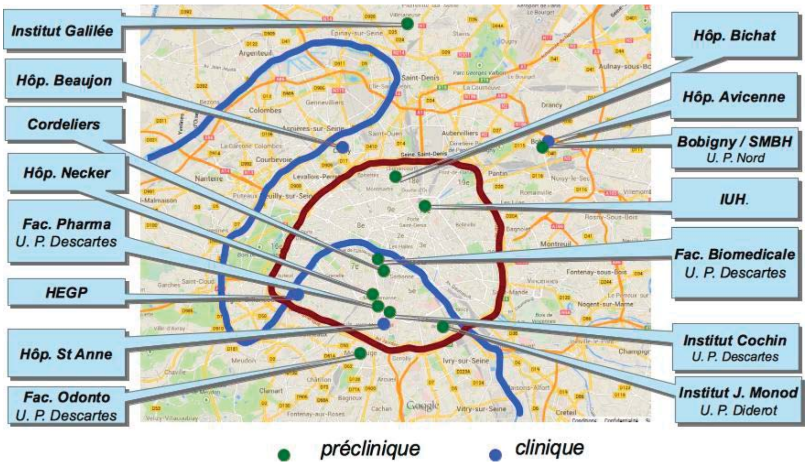

The Atlas-IDV is based on Cirrus, a USPC Big-Data facility, and more especially on the ‘Cloud-IDV’ supported by the Cumulus infrastructure (the U. Paris Descartes Cloud facility). The database is developed with a strong focus on interoperability, distributed architecture and standardization of metadata. Especially, an ontology-based dataset annotation standard is proposed, based on inputs from experts in a large number of image-based disciplines. To allow data and algorithm sharing, we use Virtual Machines (VM,150 Linux or Windowsalready allocatedVM) owned by the scientists wanting to share data sets, computing environments or commercial license keys. Basically, scientists can get ‘software VM’ (where algorithms are shared to work on the data), ‘backup VM’, and ‘Database VM’, all shared with each other. The proposed VM templatesare available are pre-equipped with a curated? set of imaging services and software elements.

To allow data and algorithm sharing, we use Virtual Machines (VM,150 Linux or Windowsalready allocatedVM) owned by the scientists wanting to share data sets, computing environments or commercial license keys. Basically, scientists can get ‘software VM’ (where algorithms are shared to work on the data), ‘backup VM’, and ‘Database VM’, all shared with each other. The proposed VM templatesare available are pre-equipped with a curated? set of imaging services and software elements.

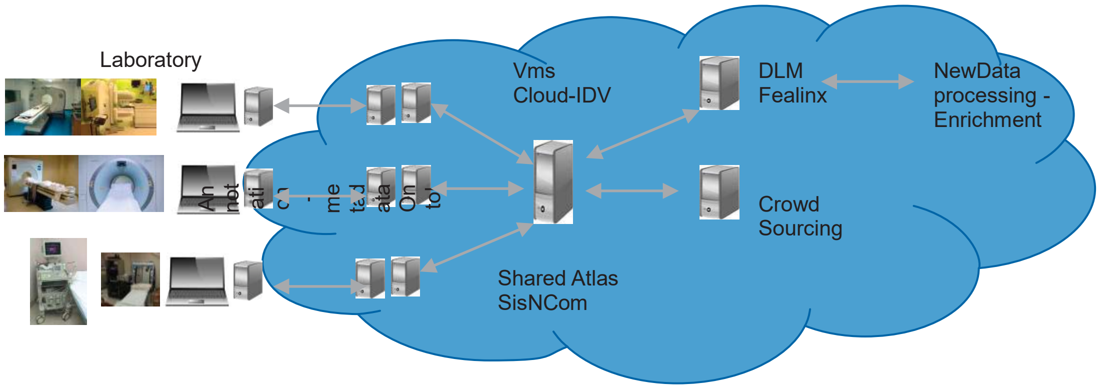

Our presentation will depict the tools developed on some trial sites for allowing data sharing, as depicted in the general scheme below :This allows sharing of data, for imaging storage and processing, coming from MRI, echography, PET, optical imaging, EPRI equipments … with a common annotation basis to improve synergy and communicationbetween the different teams of the imaging community.

This allows sharing of data, for imaging storage and processing, coming from MRI, echography, PET, optical imaging, EPRI equipments … with a common annotation basis to improve synergy and communicationbetween the different teams of the imaging community.

Sammba-MRI: An imaging toolbox for small animal imaging by MRI

Salma Bougacha[1, 2], Nachiket Nadkarni[1], Clément Garin[1], Marc Dhenain[1]
[1]Neurodegenerative Dis. Lab., MIRCen, CEA, Fontenay aux Roses Cedex, France; [2]U1077, INSERM, Caen, France

Introduction

Small mammals neuroimaging offers incredible opportunities to investigate structural and functional aspects of the brain. Many tools have been developed in the last decade to analyze small animal data, but current softwares are less mature than the available tools that process human brain data. The Python package sammba-MRI (SmAll MaMmals BrAin MRI in Python; http://sammba-mri.github.io) is designed to allow flexible and efficient use of existing methods and enables fluent scriptable analysis workflows, from DICOM conversion to results visualization.

Material and Methods

Sammba-MRI offers a toolbox to download reference neuroimaging datasets from different species of small animals. It provides end-to-end pipelines to process and analyze multimodal images, including structural, functional and perfusion MRI.

Sammba-MRI allows to convert Bruker DICOM files to the standard Nifti-1 imaging format and extracts extensive information using DCMTK. It combines different neuroimaging tools leveraged through nipype [1] to perform spatial preprocessing steps: bias-field correction with ANTS, brain extraction with RATS [2, 3], EPI distortion correction and spatial registration with AFNI. Resting state fMRI (rsfMRI) connectivity analysis is handled through nilearn [4], while perfusion map estimation uses nonlinear fitting. Finally, brain images visualization is done with nilearn.

Sammba-MRI provides practical examples to shows how to use the implemented methods. By relying on nipype interfaces, sammba-MRI is able to run an entire analysis in a single Python script. The package design facilitates data exploration: rerunning pipelines is optimized through caching mechanisms and long lasting steps are executed in parallel.

Results

We selected three examples that can be readily customized to various studies.

Studying populations of animals gains precision by the use of cohort specific templates. Sammba-MRI proposes an iterative method to create a fine anatomical template from individual structural MRI scans. We show in Figure 1 the published template [5] created from 34 mouse lemurs (15-60 months old). The method adapts to different animal species.

Estimating the cerebral blood flow (CBF) in animals is challenging due to the low SNR and lack of sensitivity. Sammba-MRI allows to estimate quantitative CBF maps for Bruker-FAIR EPI sequences. Figure 2 shows CBF map from a group of 10 mice (5-7 months old).

Resting state spatial networks extraction can be done using ICA. Using sammba-MRI, we performed ICA on a group of 15 mice (2-3 months old) from a public dataset [6]. Relevant bilateral regions are found even without data post-processing (Figures 3 and 4).

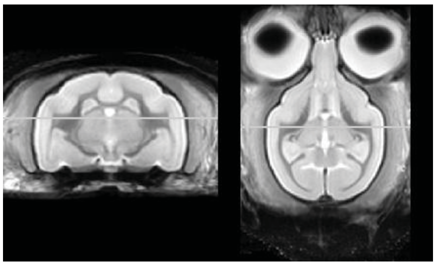	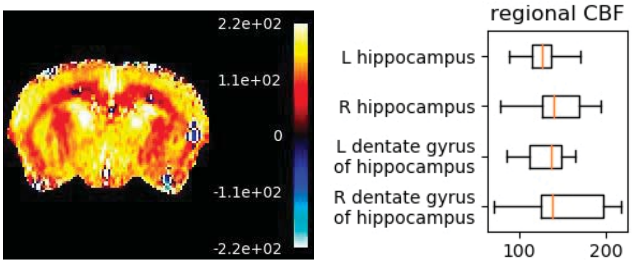	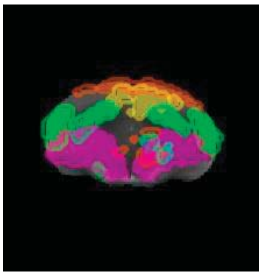
Figure 1. Mouse lemurs template.	Figure 2. Left to right : group average CBF map and individual regional CBF.	Figure 3. ICA probabilistic maps.

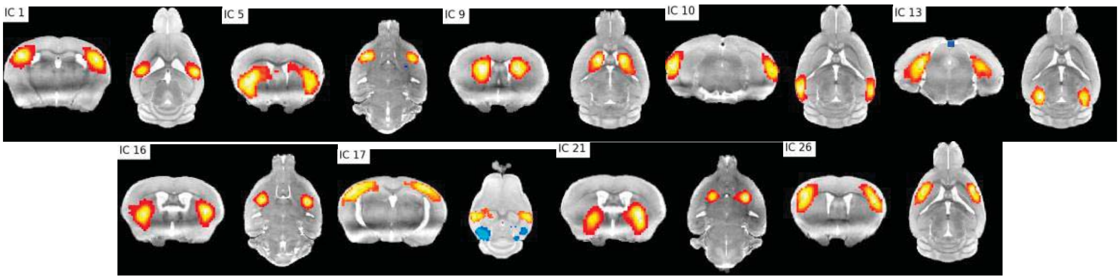	Figure 4. Bilateral ICA components.

Discussion/Conclusion

Hosted on the open GitHub platform, sammba-MRI further encourages inter-laboratory collaboration towards enhanced software quality and data-analysis protocols in the animal neuroimaging community. The researcher is provided with animal neuroimaging data and analysis tools. In this way, research discovery from animal imaging will be simplified and accelerated.

References

[1] Gorgolewski, K. et al. "Nipype: A Flexible, Lightweight and Extensible Neuroimaging Data Processing Framework in Python". *Frontiers in Neuroinformatics*, *5*, 13 (2011).

[2] Oguz, I. et al. "RATS: Rapid Automatic Tissue Segmentation in rodent brain MRI". *Journal of neuroscience methods* (2014) vol. 221 pp. 175 - 182.

[3] Yin, Y. et al. "LOGISMOS - Layered Optimal Graph Image Segmentation of Multiple Objects and Surfaces: cartilage segmentation in the knee joint". *IEEE Transactions on Medical Imaging* (2010).

[4] Abraham A. et al. "Machine learning for neuroimaging with scikit-learn". *Frontiers in Neuroinformatics 8* (2014).

[5] NADKARNI, N.A. et al. "An MRI anatomical atlas and resting state activity-based functional parcellation of the brain of the mouse lemur primate (Microcebus murinus)". *SFN* 2017.

[6] Zerbi, V. et al. "Mapping the Mouse Brain with Rs-fMRI: An Optimized Pipeline for Functional Network Identification". *NeuroImage* 123 (2015): 11–21.

Dicomifier: a generic Bruker-DICOM-NIfTI converter

Julien LAMY, Romain LAHAXE, Farid OUHMICH

ICube, Université de Strasbourg, CNRS

Introduction

When working with pre-clinical and clinical MRI data, two main formats are available: a proprietary format output by the ubiquitous Bruker pre-clinical scanners, and standard DICOM [1] data sets generated by the clinical scanners. On the image-processing side however, other, often simpler, formats are preferred, NIfTI [2] being the most obvious example in the field of neuro-imaging. Several converters between those formats already exist, but, even though they work satisfyingly for simple acquisitions, may often behave erratically for more complex acquisitions, e.g. DTI. In this paper, we present *Dicomifier*, a generic and open-source converter designed to process both pre-clinical and clinical data and to be easily extensible to account for the wealth of meta-data associated with medical images.

Design

The design of the converter is modular: one part handles the conversion from the Bruker format to the DICOM format and another part handles the conversion from the DICOM format (either native or converted from the Bruker format) to NIfTI. This modular design allows future extensions, e.g. conversion from NIfTI to DICOM to store segmentation results in a PACS.

Bruker-DICOM alignment

Similar concepts guiding the hierarchy of data exist in both Bruker and DICOM formats: patient (or subject), study (i.e. a set of exams performed for a single goal) and series (single or multiple 2D or 3D images from one acquisition). The implementation of those concepts in both formats is however largely different, and, in addition to the file-format difference, data alignment is an integral part of the conversion.

The Bruker-DICOM alignment is mapping process in which a pre-defined, modality-specific set of DICOM elements is extracted from the Bruker-format exam. The mapping may be a direct one, e.g. the field called *VisuSubjectName* in the Bruker-format exam is stored as-is in the *Patient's Name* DICOM element, or a more complex one. As an example of this latter case in MR exams, Bruker stores the resonant frequency of the spectrometer for the ^{1}H nucleus (i.e. proton) in the *VisuAcqImagingFrequency* element, while DICOM stores the strength of the B_0 magnetic field in the *MagneticFieldStrength* element, yielding the following transform: $MagneticFieldStrength = \frac{VisuAcqImagingFrequency}{\gamma}$, where γ is the gyromagnetic ratio of the ^{1}H nucleus (i.e. 42.577 $MHz.T^{-1}$). These mappings functions, as well as the way to extract the data from the Bruker element and an indication of whether the field is required, are stored in data structures which follow the modular organization of DICOM objects (e.g. the *MRDiffusion* module will store the mappings for the *DiffusionBValue*, *DiffusionGradientDirectionSequence*, and *DiffusionBMatrixSequence* elements).

NIfTI files and final meta-data

Since NIfTI stores N-dimensional data and does not impose any constraint on the file name, we chose to store NIfTI files per series, and to create those files as high-dimensional as possible. For example, a functional MRI series will be stored in a 4-D NIfTI file. When the geometry of volumes is not the same in the whole series, as is the case for localizer and multiplanar reconstruction series, the N-dimensional data must be split in lower-dimensional files with a homogeneous geometry since the

NIfTI format can only store one geometry. The fixed-size header of NIfTI cannot accommodate the wide range of meta-data stored in the DICOM format, but this meta-data may nevertheless be required for further processing, e.g. in parametric MRI which often the echo time in the bio-physical models. We chose to store the meta-data in the widespread JSON [3] format, for it is easily handled by many toolboxes while remaining human-readable.

In order to avoid the repetition of meta-data which may happen from aggregating several DICOM slices in a single, high-dimensional data-set, the content of a meta-data element is merged when all the values are the same in the data-set. For example, in a given MR series, the echo time will typically take a small set of values (a single one for classical acquisitions, and usually under 10 for multi-echo acquisitions), each of those values corresponding to a reconstructed 3D volume: for a multi-echo series stored in single-slice DICOM files, it would be wasteful to store all the duplicate data and, instead of storing $n_{echoes} \times n_{slices}$ scalar elements, we store a 2-dimensional array of dimension $n_{echoes} \times 1$. This nesting is generic with respect to the dimension of the series and the actual variability of the parameters, and provides an easy access to values of selected subsets of the N-D volume.

For native DICOM files, i.e. not converted from Bruker, a normalization step is also applied to parse the data from vendor-specific fields, when the syntax of those fields is known.

Validation

Validation of the conversion was performed on three public Bruker data sets: a phantom made of alphabet noodles glued to the plunger of a syringe, designed to validate the orientation of the axes during the conversion steps, and a rat head and Lego bricks assembly acquired with various arbitrary axes, used to validate the geometry of the converted volumes. The conversion was also successfully tested on multiple data sets coming from small animal and human (both clinical and research) scans ranging from routine acquisition to advanced research MR sequences, tough, due to the difficulty of sharing clinical data, these images are not publicly available.

Conclusion

Although developed for MRI, initial testing has been performed on other modalities (CT-Scan and nuclear medicine). The results of these initial tests are encouraging, as single- and multiple-volume acquisitions were successfully converted with minimal adjustments to the code base.

The source code [4] and the test data [5] mentioned in the previous section are freely available on GitHub. The software is cross-platform, and has been successfully deployed in Linux, macOS and Windows environments.

Acknowledgments

This work was performed by laboratories member of France Life Imaging network (grant ANR-11-INBS-0006); R. Lahaxe and F Oulmich were employed by this program. We thank Simon Loury for carrying out preliminary tests of Dicomfier and interesting discussions during the course of its development.

References

[1] DICOM: Digital Imaging and Communications in Medicine, http://www.dicomstandard.org/current/
[2] NIfTI, https://nifti.nimh.nih.gov/
[3] The JSON Data Interchange Standard, ECMA-404, December 2017
[4] Dicomifier, https://github.com/lamyj/dicomifier
[5] Test data for Dicomifier, https://github.com/fli-iam/dicomifier-data

France Life Imaging (FLI) - Information Analysis and Management (IAM)

Provider of data storage and processing solutions for preclinical imaging studies

Michael Kain, INRIA Rennes, Campus Universitaire de Beaulieu
35042 Rennes Cedex – France and the FLI-IAM consortium

Abstract

Animal population imaging is a domain still in its infancy that requires a similar technical support as for human population imaging: technical solutions for storing and processing large volumes of data in a distributed scientific work environment. This challenge has been identified by the national French action FLI-IAM (https://portal.fli-iam.irisa.fr). IAM (Information Analysis and Management) is the computation science node of France Life Imaging (FLI). It provides access to multiple imaging databases and computation resources and takes care of the interoperability between databases[1] and processing pipelines (local or cluster-based platforms). The preclinical work group within FLI-IAM has especially worked on a solution for hosting preclinical imaging studies, that is called Shanoir[2] Small Animal.

We will present the FLI-IAM architecture (fig. 1) and detail our Small Animal Shanoir (SAS) solution for hosting preclinical imaging studies (fig. 2, 3): data storage and processing execution and results integration via VIP[3]/Boutiques[4].

Shanoir Small Animal provides:

- Control over the distribution and sharing of data
- Manages study meta-data and preclinical images using a specific ontology
    - Pathology models, therapies, anaesthetics and physiological data
- Import of Bruker and DICOM file formats (additional formats will be supported to comply with the evolution of the ecosystem)
- Secures online data sharing and data reuse
- Provides a storage of all research data in the cloud
- Original images + processing (code) + processed results
- Processes preclinical images on high performance systems, if required
- Support to integrate your data analysis pipeline and algorithms
- Enriches data with links using DOIs to Open Access, e.g. OpenAIRE

Currently FLI-IAM works on a new version of Shanoir called Shanoir-NG, with a completely new technological stack and architecture based on micro-services. We will detail the features of this new version and show how sharing of data and starting of pipelines work.

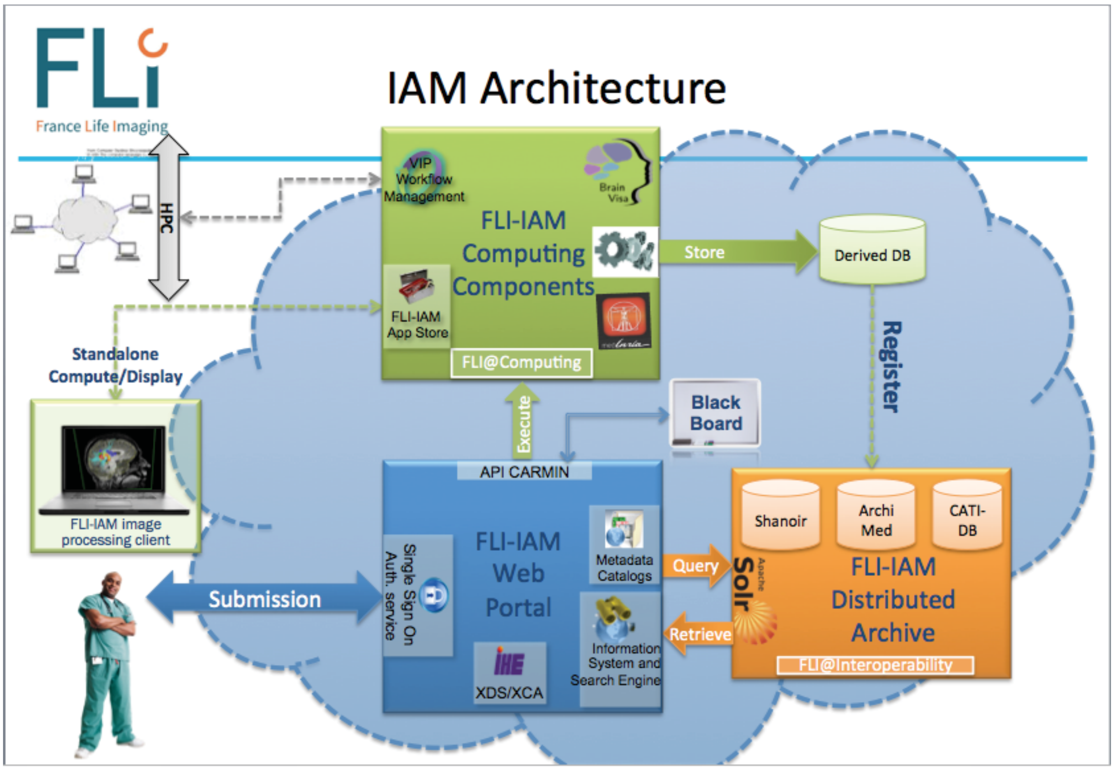

Figure 1. Architecture overview of FLI-IAM

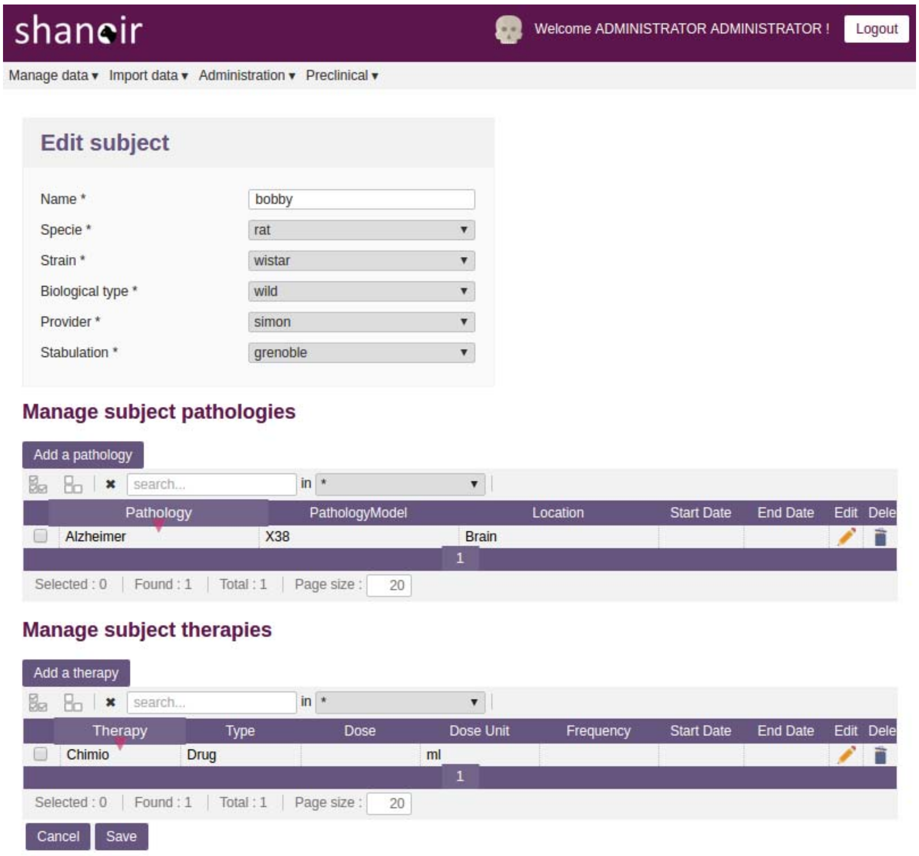

Edit subject

Name *	bobby
Specie *	rat
Strain *	wistar
Biological type *	wild
Provider *	simon
Stabulation *	grenoble

Manage subject pathologies

search... in *

	Pathology	PathologyModel	Location	Start Date	End Date	Edit	Dele
☐	Alzheimer	X38	Brain			✎	🗑

1

Selected : 0 | Found : 1 | Total : 1 | Page size : 20

Manage subject therapies

search... in *

	Therapy	Type	Dose	Dose Unit	Frequency	Start Date	End Date	Edit	Dele
☐	Chimio	Drug		ml				✎	🗑

1

Selected : 0 | Found : 1 | Total : 1 | Page size : 20

Figure 2. Shanoir-NG Small Animal, snapshot of the management of an animal subject

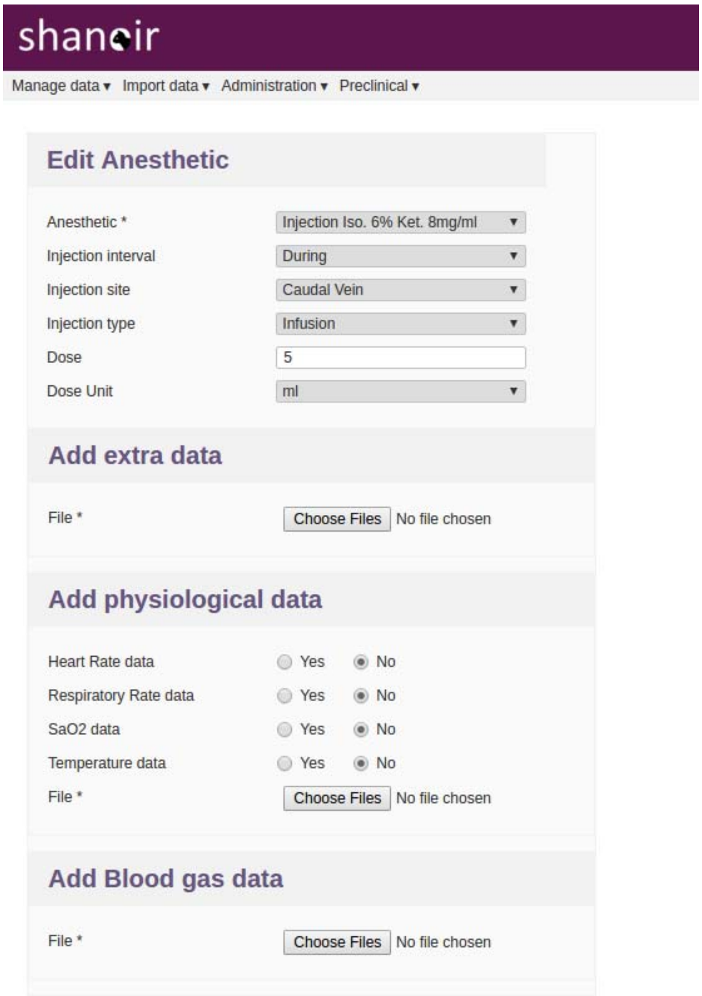

Edit Anesthetic

Anesthetic *	Injection Iso. 6% Ket. 8mg/ml
Injection interval	During
Injection site	Caudal Vein
Injection type	Infusion
Dose	5
Dose Unit	ml

Add extra data

File * Choose Files No file chosen

Add physiological data

Heart Rate data	○ Yes ● No
Respiratory Rate data	○ Yes ● No
SaO2 data	○ Yes ● No
Temperature data	○ Yes ● No
File *	Choose Files No file chosen

Add Blood gas data

File * Choose Files No file chosen

Figure 3. Shanoir-NG Small Animal, snapshot of an examination

References

1. Dojat M, Kennedy DN and Niessen W (2017) Editorial: MAPPING: MAnagement and Processing of Images for Population ImagiNG. Front. ICT 4:18. doi: 10.3389/fict.2017.00018

2. Barillot C, Bannier E, Commowick O, Corouge I, Baire A, Fakhfakh I, Guillaumont J, Yao Y and Kain M (2016) Shanoir: Applying the Software as a Service Distribution Model to Manage Brain Imaging Research Repositories. Front. ICT 3:25. doi: 10.3389/fict.2016.00025

3. Tristan Glatard, Carole Lartizien, Bernard Gibaud, Rafael Ferreira da Silva, Germain Forestier, et al.. A virtual imaging platform for multi-modality medical image simulation.. IEEE Transactions on Medical Imaging, Institute of Electrical and Electronics Engineers, 2013, 32 (1), pp.110-8. doi: 〈10.1109/TMI.2012.2220154〉 . 〈inserm-00762497〉

4. Glatard T, Da Silva RF, Boujelben N, ADALAT R, Beck N, Rioux P, Rousseau M, Deelman E and Evans AC (2015). Boutiques: an application-sharing system based on Linux containers. . Front. Neurosci. Conference Abstract: Neuroinformatics 2015. doi: 10.3389/conf.fnins.2015.91.00012

Development of a configurable workflow for processing preclinical images

Sara Zullino, Walter Dastrù, Silvio Aime and Dario Longo

Molecular Imaging Center, Department of Molecular Biotechnologies and Health Sciences,
University of Torino, Torino, Italy

Introduction

Available medical imaging data can be a highly valuable resource for research on diagnostics, epidemiology and drug development. This has also prompted increasing interest in the development of data driven models based on computational approaches and image processing algorithms. A common limitation to this process is dependent on the complexity of the processing, on the elevate number of 3D images to be processes and on the lack of common tools for sharing and processing medical images obtained by different imaging centres and/or acquired with different imaging instrumentations vendors. This can be explained in part by a lack of free access to medical imaging data for research, preventing the development of robust image processing methods and by the requested computational resources. As a consequence, successful analysis of imaging data in the medical context requires a multidisciplinary effort, integrating ad-hoc archiving platforms, providing these data in shared databases and developing optimized processing tools to extract a large number of quantitative features from digital images.

Within this project we aim to develop tools for easily extracting, importing, archiving preclinical image data from several imaging device manufacturers and to implement tools for automated image processing. The herein developed workflow for preclinical images will be made available to the wide preclinical research community, hence allowing a simplified exchange and (re)use of image datasets between preclinical imaging centres.

Materials and Methods

Python-based tools, implementing Pydicom (a Python package for reading and manipulating DICOM files) have been developed for reading, importing and archiving preclinical images This tool is intended to be embedded in the "Extensible Neuroimaging Archive Toolkit" (XNAT), an increasingly used open source platform for managing, exploring, and sharing neuroimaging data [2]. Since preclinical instrumentations usually do not match any specific standard regarding data storage and each vendor adopts a proprietary format for its data, we developed python-based tools for converting raw images coming from several vendors (to date: MRI Bruker and Aspect Imaging) to DICOM format.

The workflow is based on the following steps (**Figure 1**):

1. an archiving/searching/retrieving step for merging and collecting multiple image datasets coming from several modalities;
2. a Bruker/Aspect to DICOM format converter to upload images to XNAT;
3. an image processing step producing parametric images related to biological aspects;
4. an intermediate image processing step to extract features related to both raw and parametric images.

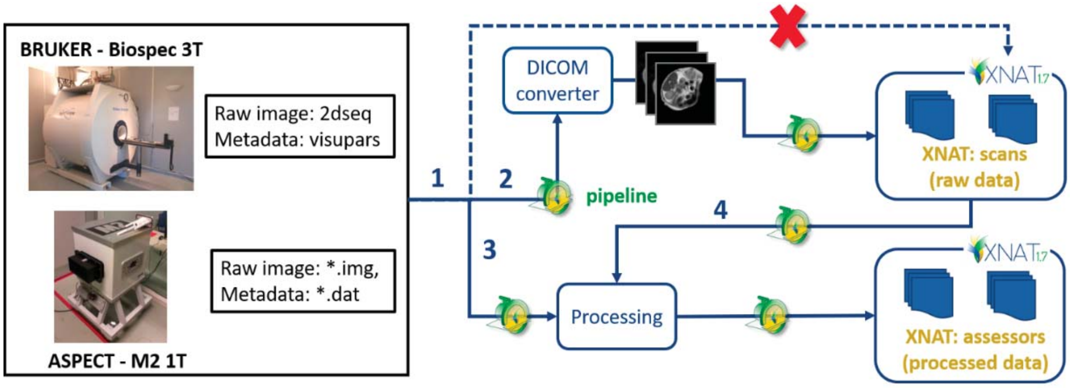

Figure 1: Schematic workflow for image archiving and processing

Results

We have developed python-based tools for (i) accessing to image raw data stored in MRI preclinical scanners, (ii) sorting the parameters of the native image format into a Python dictionary, (iii) converting raw binary images into DICOM format and iv) storing the meaningful information into the DICOM header (tags) and image set field (**Figure 2**). XNAT pipelines have been implemented to load large datasets of data arising from several studies/patients/sessions into DICOM images by preserving a meaningful tree-like structure (**Figure 3**).

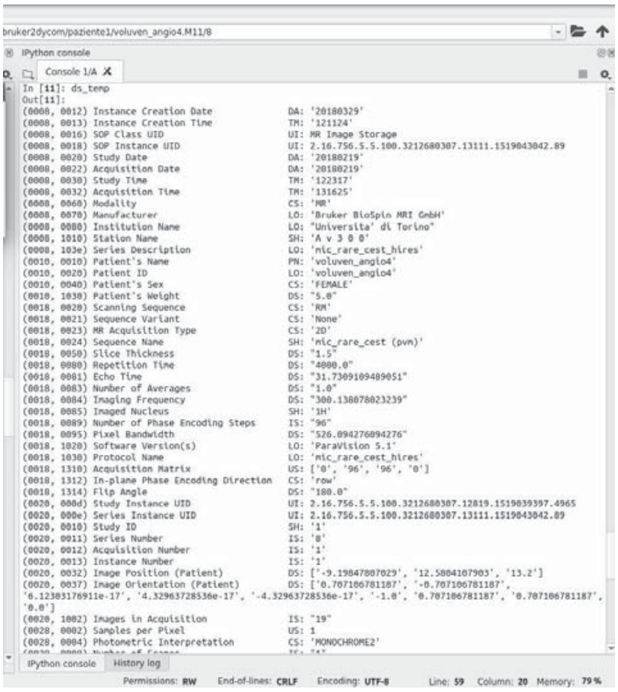

```
In [11]: ds_temp
Out[11]:
(0008, 0012) Instance Creation Date              DA: '20180329'
(0008, 0013) Instance Creation Time              TM: '121124'
(0008, 0016) SOP Class UID                       UI: MR Image Storage
(0008, 0018) SOP Instance UID                    UI: 2.16.756.5.5.100.3212680307.13111.1519043042.89
(0008, 0020) Study Date                          DA: '20180219'
(0008, 0022) Acquisition Date                    DA: '20180219'
(0008, 0030) Study Time                          TM: '122317'
(0008, 0032) Acquisition Time                    TM: '131625'
(0008, 0060) Modality                            CS: 'MR'
(0008, 0070) Manufacturer                        LO: 'Bruker BioSpin MRI GmbH'
(0008, 0080) Institution Name                    LO: "Universita' di Torino"
(0008, 1010) Station Name                        SH: 'A v 3 0 0'
(0008, 103e) Series Description                  LO: 'mic_rare_cest_hires'
(0010, 0010) Patient's Name                      PN: 'voluven_angio4'
(0010, 0020) Patient ID                          LO: 'voluven_angio4'
(0010, 0040) Patient's Sex                       CS: 'FEMALE'
(0010, 1030) Patient's Weight                    DS: "5.0"
(0018, 0020) Scanning Sequence                   CS: 'RM'
(0018, 0021) Sequence Variant                    CS: 'None'
(0018, 0023) MR Acquisition Type                 CS: '2D'
(0018, 0024) Sequence Name                       SH: 'mic_rare_cest (pvm)'
(0018, 0050) Slice Thickness                     DS: "1.5"
(0018, 0080) Repetition Time                     DS: "4000.0"
(0018, 0081) Echo Time                           DS: "31.7309109489051"
(0018, 0083) Number of Averages                  DS: "1.0"
(0018, 0084) Imaging Frequency                   DS: "300.138078023239"
(0018, 0085) Imaged Nucleus                      SH: '1H'
(0018, 0089) Number of Phase Encoding Steps      IS: "96"
(0018, 0095) Pixel Bandwidth                     DS: "526.094276094276"
(0018, 1020) Software Version(s)                 LO: 'ParaVision 5.1'
(0018, 1030) Protocol Name                       LO: 'mic_rare_cest_hires'
(0018, 1310) Acquisition Matrix                  US: ['0', '96', '96', '0']
(0018, 1312) In-plane Phase Encoding Direction   CS: 'row'
(0018, 1314) Flip Angle                          DS: "180.0"
(0020, 000d) Study Instance UID                  UI: 2.16.756.5.5.100.3212680307.12819.1519039397.4965
(0020, 000e) Series Instance UID                 UI: 2.16.756.5.5.100.3212680307.13111.1519043042.89
(0020, 0010) Study ID                            SH: '1'
(0020, 0011) Series Number                       IS: '8'
(0020, 0012) Acquisition Number                  IS: '1'
(0020, 0013) Instance Number                     IS: '1'
(0020, 0032) Image Position (Patient)            DS: ['-9.19847807029', '12.5804107903', '13.2']
(0020, 0037) Image Orientation (Patient)         DS: ['0.707106781187', '-0.707106781187',
'6.12303176911e-17', '4.32963728536e-17', '-4.32963728536e-17', '-1.0', '0.707106781187', '0.707106781187',
'0.0']
(0020, 1002) Images in Acquisition               IS: "19"
(0028, 0002) Samples per Pixel                   US: 1
(0028, 0004) Photometric Interpretation          CS: 'MONOCHROME2'
```

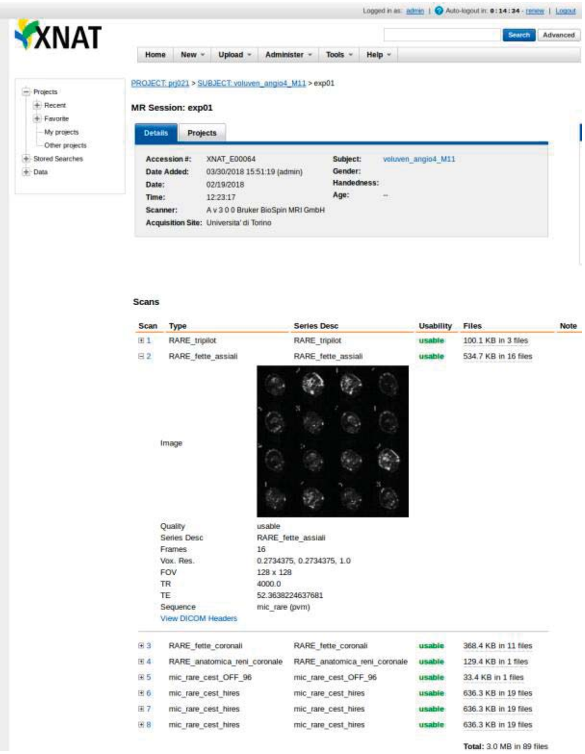

PROJECT: prj021 > SUBJECT: voluven_angio4_M11 > exp01

MR Session: exp01

Accession #: XNAT_E00064
Date Added: 03/30/2018 15:51:19 (admin)
Date: 02/19/2018
Time: 12:23:17
Scanner: A v 3 0 0 Bruker BioSpin MRI GmbH
Acquisition Site: Universita' di Torino
Subject: voluven_angio4_M11
Gender:
Handedness:
Age: --

Scans

Scan	Type	Series Desc	Usability	Files	Note
⊞ 1	RARE_tripilot	RARE_tripilot	usable	100.1 KB in 3 files	
⊟ 2	RARE_fette_assiali	RARE_fette_assiali	usable	534.7 KB in 16 files	

Image
Quality: usable
Series Desc: RARE_fette_assiali
Frames: 16
Vox. Res.: 0.2734375, 0.2734375, 1.0
FOV: 128 x 128
TR: 4000.0
TE: 52.3638224637681
Sequence: mic_rare (pvm)

Scan	Type	Series Desc	Usability	Files	Note
⊞ 3	RARE_fette_coronali	RARE_fette_coronali	usable	368.4 KB in 11 files	
⊞ 4	RARE_anatomica_reni_coronale	RARE_anatomica_reni_coronale	usable	129.4 KB in 1 files	
⊞ 5	mic_rare_cest_OFF_96	mic_rare_cest_OFF_96	usable	33.4 KB in 1 files	
⊞ 6	mic_rare_cest_hires	mic_rare_cest_hires	usable	636.3 KB in 19 files	
⊞ 7	mic_rare_cest_hires	mic_rare_cest_hires	usable	636.3 KB in 19 files	
⊞ 8	mic_rare_cest_hires	mic_rare_cest_hires	usable	636.3 KB in 19 files	

Total: 3.0 MB in 89 files

Figure 2. *Screenshot with DICOM metadata extracted from raw images (left)*
Figure 3. *Corresponding XNAT loaded preclinical images stored (right).*

Conclusions

An easy-to-use, adaptable and implementable workflow has been developed to load raw images arising from preclinical imaging centers into a XNAT-based archive system. The advantage of this approach relies in the capability to operate with several imaging modalities and in the capability to easily apply different image processing analysis procedures to the same datasets.

References

[1] Mason, D. (2011), SU-E-T-33: Pydicom: An Open Source DICOM Library. Med. Phys., 38: 3493-3493.
[2] D. S. Marcus, T. R. Olsen, M. Ramaratnam, and R. L. Buckner, "The extensible neuroimaging archive toolkit: An informatics platform for managing, exploring, and sharing neuroimaging data," Neuroinformatics, 2007, 5, 11–33

Multi-center resting-state fMRI comparison reveals common functional networks in the mouse brain.

Joanes GRANDJEAN[a], Carola CANELLA[b,c], Cynthia ANCKAERTS[d], Gülebru AYRANCI[h], Ludovico COLETTA[b,c], Daniel GALLINO[h], Natalia GASS[e], Neele HÜBNER[f], Silke KREITZ[k], Francesca MANDINO[ao], Anna E. MECHLING[f], Sandra STROBELT[k], Tong WU[g,i], Isabel WANK[k], Ling Yun YEOW[a], Yohan YEE[p], Mallar CHAKRAVARTY[h], Wei-Tang CHANG[a], Dominik VON ELVERFELDT[f], Laura-Adela HARSAN[j], Andreas HESS[k], Georgios A. KELIRIS[d], Jason LERCH[p], Markus RUDIN[l], Alexander SARTORIUS[e], Tianzi JIANG[g,m], Annemie VAN DER LINDEN[d], Marleen VERHOYE[d], Wolfgang WEBER-FAHR[e], Nicole WENDEROTH[n], Valerio ZERBI[n], Alessandro GOZZI[b].

a Singapore BioImaging Consortium, Agency for Science, Technology and Research, 11 Biopolis Way, Singapore 138667, Singapore
b Functional Neuroimaging Laboratory, Istituto Italiano di Tecnologia, Center for Neuroscience and Cognitive Systems @ UNITN, 38068 Rovereto, Italy
c CIMeC, Center for Mind/Brain Sciences, University of Trento, 38068 Rovereto, Italy
d Bio-Imaging Lab, University of Antwerp, CDE, Universiteitsplein 1, 2610 Antwerp, Belgium
e Department of Neuroimaging, Central Institute of Mental Health, Medical Faculty Mannheim, University of Heidelberg, Mannheim, Germany
f Advanced Molecular Imaging Research Center (AMIR), Medical Physics, Department of Radiology, University Medical Center and the BrainLinks-BrainTools Cluster of Excellence, University of Freiburg, 79106 Freiburg, Germany
g Queensland Brain Institute, The University of Queensland, Brisbane, Queensland, Australia
h Douglas Mental Health University Institute & Departments of Psychiatry and Biological and Biomedical Engineering, McGill University, Montreal, QC, Canada.
i Centre for Medical Image Computing, Department of Computer Science, & Max Planck University College London Centre for Computational Psychiatry and Ageing Research, University College London, UK
j Department of Biophysics and Nuclear Medicine, University Hospital Strasbourg, 67000 Strasbourg, France
k Friedrich-Alexander University Erlangen-Nürnberg (FAU), Institute of Experimental and Clinical Pharmacology and Toxicology, Fahrstraße 17, 91054, Erlangen, Germany
l Institute for Biomedical Engineering, University and ETH Zürich, Wolfgang-Pauli-Str. 27, 8093 Zürich, Switzerland, & Institute of Pharmacology and Toxicology, University of Zürich, Winterthurerstrasse 190, 8057 Zürich, Switzerland
m Brainnetome Centre, Institute of Automation, Chinese Academy of Sciences, Beijing & Key Laboratory for NeuroInformation of the Ministry of Education, School of Life Science and Technology, University of Electronic Science and Technology of China, Chengdu 625014, China
n Neural Control of Movement Lab, HEST, ETH Zürich, Winterthurerstrasse 190, 8057 Zurich, Switzerland
o Faculty of Life Sciences, University of Manchester, Manchester, United Kingdom
p Hospital for Sick Children, Toronto, Ontario, Canada

Introduction: Resting-state functional magnetic resonance imaging (rs-fMRI) has brought considerable understanding onto the nature of the brain organization and function, and remains, to date, a central method in neuroimaging. Functional connectivity (FC) estimated in the mouse brain using rs-fMRI is a fast-developing field holding the exciting promise to uncover the basic principles of large-scale functional organization, as well as the mechanisms leading to their alterations under pathological conditions (for review see [1-4]). Since its formal onset in 2011 [5], the method has been adopted by several laboratories world-wide. Similar to functional imaging acquired in human, acquisitions in rodents are carried at varying field strengths, coil configurations, and sequences. In addition, differences in animal handling procedures may further impact results, preventing a comparison of published results between laboratories, and complicating the establishment of standardized methods for preclinical imagers. We have carried out a multi-centre comparison of 12 datasets representative of the protocols obtained in the respective laboratories using a common data analysis pipeline. Specifically, we aim to investigate the reproducibility of murine functional networks across centres.

Material and Methods: 12 datasets consisting of 15 individual rs-fMRI scans were acquired with gradient-echo echo planar imaging (EPI). Scans were acquired on dedicated Bruker magnets operating at 4.7T (N=1 dataset), 7T (N=4), 9.4T (N=6), 11.7T (N=1), with either room-temperature coils (N=5) or cryocoils (N=7). All acquisitions were performed on anesthetized C57B6/J mice (both male and female) with either isoflurane 1-1.2% (N=4), halothane 0.75% (N=1), medetomidine 0.1-0.4 mg/kg bolus and 0.2-0.8 mg/kg/h infusion (N=2), or a combination of isoflurane 0.2-0.5% and medetomidine 0.05-0.3mg/kg bolus and 0-0.1 mg/kg/h infusion (N=5). Animals were either freely-breathing (N=7) or mechanically ventilated (N=5). All data was pre-processed using an adapted pipeline based on FSL FEAT [6]. A number of denoising approaches were compared; results are shown following vascular and ventricular signal regression. FC data analysis was performed using several commonly used approaches: seed-based analysis (SBA), independent component analysis, and ROI-based network analysis. Detailed results in this abstract are provided for SBA. Statistical FC maps across datasets were obtained with permutation-based one-sample t-tests using cluster correction. Within-dataset statistical FC maps were obtained with parametric one-sample t-tests and are reported as significance incidence ($p<0.05$, uncorrected) across datasets.

Results: Individual scans displayed minimal geometric distortions. Cortical signal-to-noise ratio (SNR) ranged from 29.7±2.7 to 298.9±34.6. There was a positive association between field strength and SNR ($p=1.7\times10^{-8}$), and between coil type (room-temperature or cryocoil) and SNR ($p=0.0061$). Maximal motion in most scans was kept below 10% of the voxel dimension. Seeds positioned in representative anatomical regions of the left hemisphere revealed the spatial extent of murine resting-state networks, indicating a bilateral organisation (Insular area, motor area, hippocampus, striatum, thalamus seeds), as well as a rostro-caudal organisation together with bilateral posterior parietal cortical regions when an anterior cingulate seed was used. This latter network recapitulates anatomical features reminiscent of the human default-mode network (Fig. 1)[7]. Considered individually, 60-80% of the datasets presented significant contralateral FC for the insular seed. FC reproducibility for to the anterior cingulate seed presented lower incidence, ranging between 40-60%, in distal posterior parietal cortical areas.

Individual FC values were extracted either from a contralateral region-of-interest (ROI) for the insular seed or a ROI located in the retrosplenial area for the anterior cingulate seed. These FC data were further investigated in depth within a linear model approach including factors related to equipment, acquisition, and animal handling. In both ROIs, anaesthesia was identified as a significant explanatory factor (p= 1.3e-5 for insular area, p= 1.0e-7 for retrosplenial area). Mechanical ventilation presented a strong effect on FC with respect to the cingulate seed (p= 2.5e-5 for retrosplenial area, p= 0.12, for insular area). Finally, SNR, used as a proxy of field strength X coil setup X sequence interactions, only reached significance effect on the FC for the insular area (p= 2.4e-13) but not in the retrosplenial ROI (p= 0.28).

Discussion: Representative datasets from imaging centres world-wide revealed robustness and spatial extent of commonly investigated functional networks in the mouse brain. With the growing body of literature regarding FC in mice, this study allows a crucial comparison of datasets to investigate the basis of FC in the healthy and diseased brain. While the spatial extents of resting-state networks converged, divergences remained in long-range rostro-caudal connectivity, encompassing regions associated with the rodent default-mode network. Careful protocol planning and comparisons with the standards established in this study will serve as a key reference for rs-fMRI mapping in the mouse, and will guide the future design of more robust protocols.

References: **(1)**.Jonckers, E., et al., Front Pharmacol, 2015. 6: p. 231. **(2)**.Pan, W.J., et al., Front Neurosci, 2015. 9: p. 269. **(3)**.Gozzi, A. and A.J. Schwarz, Neuroimage, 2016. 127: p. 496-509. **(4)**.Chuang, K.H. and F.A. Nasrallah, Neuroimage, 2017. **(5)**.Jonckers, E., et al.,. PLoS One, 2011. 6(4): p. e18876. **(6)**.Zerbi, V., et al., Neuroimage, 2015. 123: p. 11-21. **(7)**.Sforazzini, F., et al., Neuroimage, 2014. 87: p. 403-15.

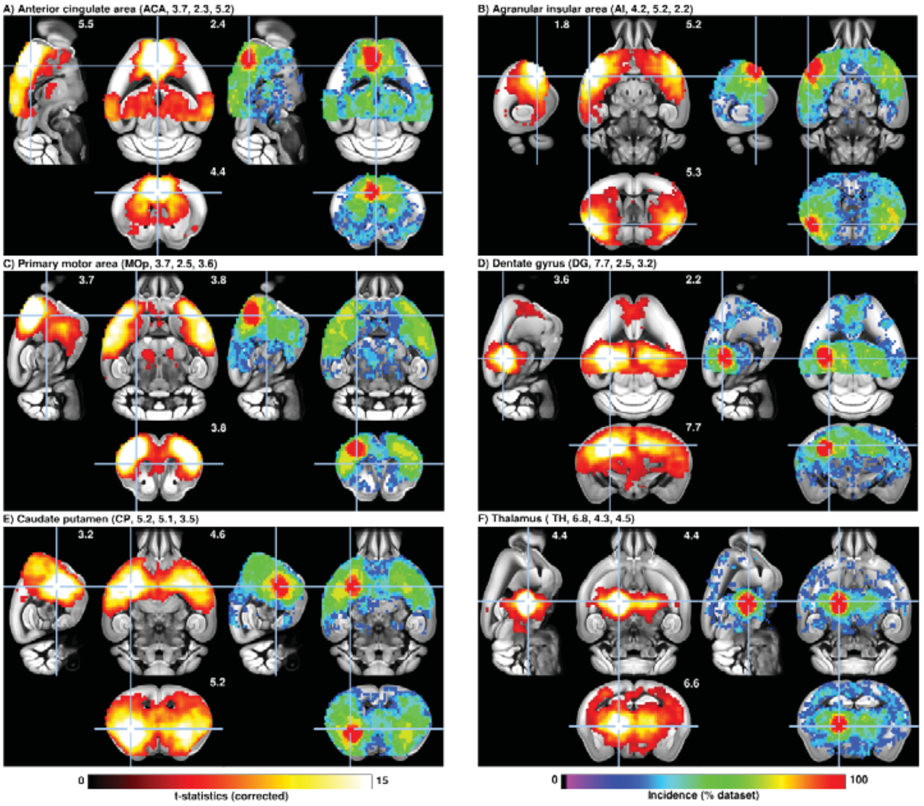

Figure 1 | Seed-based resting-state networks for 6 representative seeds shown as one-sample t-statistics ($p<0.05$, cluster-corrected, left) and reproducibility between datasets shown as incidence maps (right). Mouse resting-state FC maps presented a robust homotopic extension with respect to the strong bilateral organization for most seeds, except for the anterior cingulate cortical seed, which also displayed a stronger rostro-caudal organisation. The spatial extent reproducibility of these maps ranged between 60-80% contralateral to the majority of seeds, and 40-60% along the rostro-caudal axis for the anterior cingulate seed.

MULTI-CENTER QUANTITATIVE MAPPING OF T1 AND T2 RELAXATION TIMES IN THE RAT BRAIN

Tristan Deruelle[1], Adriana Perles-Barbacaru[2], Franck Kober[2], Thierry Delzescaux[3], Emmanuel L. Barbier[1], Michel Dojat[1]
[1]Univ. Grenoble Alpes, INSERM, CHU Grenoble Alpes, GIN, 38000 Grenoble, France
[2] Aix-Marseille Univ, CNRS, CRMBM, 13385 Marseille, France
[3] UMR-9199, CNRS, CEA-MIRCEN, 92265 Fontenay-Aux-Roses, France

Introduction *In vivo* T1 and T2 relaxation times are tissue dependent and their modifications may be characteristic of specific anatomical regions and pathological situations. The aim of this project was to produce quantitative 3D T1 and T2 maps for the healthy rat brain that can eventually be used as normative references. Such maps were defined based on data acquired at two different centers GIN and CRMBM with three different image processing pipelines. We report on the differences obtained and discuss the feasibility of running multi-center preclinical studies.

Methods

Animals. Ten Sprague Dawley (5-6 weeks old) were used in each center GIN and CRMBM (different animal at GIN and at CRMBM). For reproducibility testing, the rats were imaged twice at GIN (referred as GIN & GIN_2; delay: 1 month). The rats were anaesthetized with 2% isoflurane. They were spontaneously breathing throughout the entire experiment. Breath rate was monitored using a pressure sensor and a monitoring unit. Body temperature was monitored with a rectal probe and maintained in the normal range using a heated blanket. All procedures were approved by a local ethical review committee.

MRI. All the images were acquired using a 7 T horizontal scanners (Bruker Biospin, Ettlingen, Germany) in the two centers. Radiofrequency (RF) transmission was done with a volume coil (diameter: 72 mm). A circular receiver surface coil (diameter: 24 mm) was placed above the dorso-caudal part of the brain. For T1 mapping, a MP-RAGE sequence was used with eight inversion times (TI) (150, 247, 408, 674, 1112, 1838, 3030, and 5000 ms). Those values were chosen so that they were equally distributed along the y-axis of an exponential curve. For T2 mapping, a MSME sequence was used with 28 echo times (from 8 to 224 ms), TR=600 ms, FOV was 2.7x2.7x2.8 cm^3 and spatial resolution 211x211x424 μm^3 (acquisition matrix 128x128x66).

Data Analysis. All individual data were first realigned (rigid body transformation) using SPM12. As SPM was initially developed for Human, the images were firstly rescaled by a multiplicative factor of 10. Using one T1-weighted image, SPM12 tissues segmentation was performed and brain extracted for each animal. The image was then parceled using a multi-atlas approach (1). Using two formal expressions of pixel intensity, depending on TI or TE, a non-linear fitting function provided T1 or T2 maps (2,3). Three fitting pipelines developed independently by each partner (GIN, CRMBM and MIRCEN) were tested. No information was exchanged about the pipelines, which relied respectively on Matlab, ImageJ and BrainVISA functions, and were considered as "black boxes". Each center provided its own pipeline. For each center and each pipeline, T1 and T2 values in each voxel were averaged across each parcel and each animal. All data were stored on Shanoir_SA, a platform for sharing neuroimaging data. Image processing pipelines were embedded into Docker containers and executed on the VIP processing platform.

Results

Figure 1 shows the different T1 values for each center, CRMBM and GIN, computed with the three pipelines. No differences between GIN and CRMBM pipelines results were observed (p>0.84). MIRCEN provided lower values (200 ms less). Regarding reproducibility, GIN_2 results tended to be lower for all pipelines (p<0.002) but the MIRCEN pipeline. For T2 values, regardless of the data origin, all pipelines computed similar values). Here, measurement reproducibility was ensured (no difference between GIN and GIN_2 differences, p>0.92). Major results are summarized in the T1 vs T2 plot (Figure 2). T1 and T2 values are grouped for each data center (low intra-center variability). T1 values computed using the MIRCEN pipeline are clearly lower than those computed with GIN or CRMBM pipelines, while T2 values were comparable for all pipelines for the two data providers, with lower values for CRMBM compared to GIN. Intra-center reproducibility (GIN) was better for T2 than for T1 values. The comparison with the literature (4,5,6,7) indicates a good correspondence for all regions for T2 values and T1 values computed with GIN or CRMBM pipelines, except Amygdala and Hippocampus.

Discussion

This work investigates the influence of data acquisition centers (n=2) and image processing pipelines (n=3) on the production of T1 and T2 brain maps. It demonstrates the coherence of the final computed maps when the acquisition sequence parameters are optimized and harmonized between centers. Additional investigations should be performed to understand the differences obtained for T1 values with one of the pipelines (MIRCEN). The inter-individual intra-center results are similar in average for T1 and T2 values. Correlation of mean values in the ROIs between centers is very good for T1 ($r^2>0.9$) with an almost linear relation (factor of 1.1), and good for T2 ($r^2 > 0.78$, factor by 1.8). The poor reproducibility for T1 values in one of the centers (GIN) is certainly due to physiological changes (weight and age) in the animals between the scanning sessions. This study demonstrates the feasibility of pooling animal data from different centers and the use of a distributed computing architecture for image storage and processing pipeline execution, paving the way for multi-center preclinical studies.

Acknowledgments

This work was performed by laboratories member of France Life Imaging network (grant ANR-11-INBS-0006) and T. Deruelle is recipient of a grant from this program. We thank Youssef Alidrissi for carrying out preliminary investigations on the topic.

References

(1) S. Lancelot *et al.*, *PLoS One*, vol. 9, no. 10, p. e109113, 2014.
(2) J. V Liu et al. *NeuroImage*, vol. 56, no. 3, pp. 1154–1163, 2011.
(3) R. Metere et al. *PLoS One*, vol. 12, no. 1, pp. 1–28, 2017.
(4) E. L. Barbier *et al.*, *NMR Biomed.*, vol. 18, no. 8, pp. 499–506, 2005.
(5) M. R. Del Bigio et al. *Fluids Barriers CNS*, vol. 8, no. 1, pp. 1–13, 2011.
(6) V. Gigliucci *et al.*, *Eur. Neuropsychopharmacol.*, vol. 24, no. 8, pp. 1349–1361, 2014.
(7) M. Behroozi *et al.*, *Magn. Reson. Med.*,79(2):1090-1100, 2018.

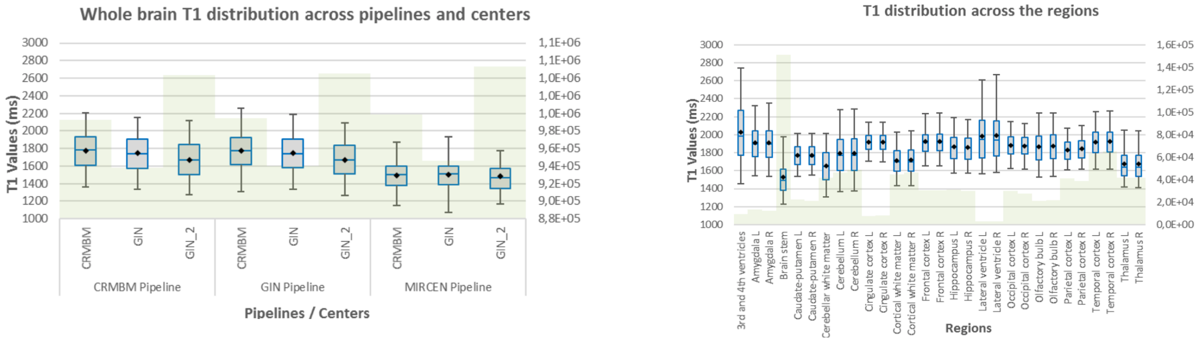

Figure 1: T1 values. Left: T1 values computed by three pipelines on data from two centers CRMBM and GIN on ten rats. Rats were imaged twice at GIN (GIN, GIN_2). Right: T1 values in different brain regions using the CRMBM pipeline for CRMBM data. Light green color indicates the number of voxels (corresponding y-axis at right) considered in each case.

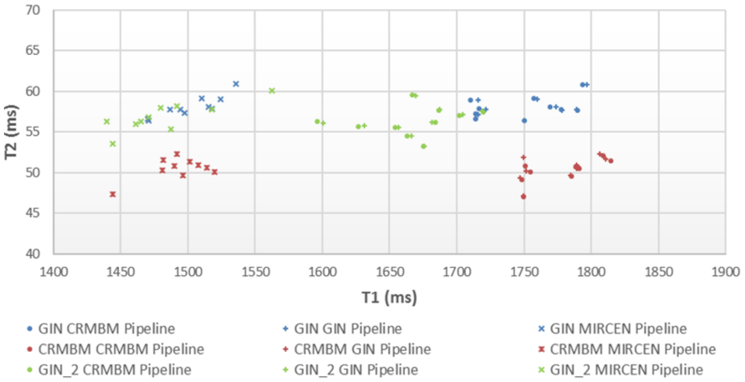

Figure 2: T2 vs T1. Values computed from three pipelines (‘+’ for GIN, ‘°’ for CRMBM, ‘x’ for MIRCEN) for the data acquired in two centers (GIN in blue, CRMBM in red). The second session at GIN is shown in green.

Impact of perfusion level on the amplitude of resting-state BOLD fMRI in anesthetized rats

Guillaume Becq[1], Sophie Achard[1], Tarik Habet[2], Nora Collomb[2], Margaux Faucher[2], Chantal Delon-Martin[2], Véronique Coizet[2], Emmanuel L. Barbier[2]

[1]GIPSA-Lab, CNRS, Université Grenoble Alpes, Grenoble, France.
[2]GIN, Inserm, Université Grenoble Alpes, Grenoble, France

Introduction

In the context of preclinical imaging, one generally uses anesthesia to restrain the animal while in the MRI scanner. One can choose its anesthesia based on EEG measurements, which estimate the brain activity level. But anesthesia also modulates the cerebral blood flow (CBF) and thereby may modulate the amplitude of BOLD signals. It is thus of interest to search for the influence of the perfusion on signals at different frequencies and with physiological measurements, depending on the anesthetic.

Materials and Methods

Groups: 5 groups of rats were considered. One group of Wistar rats, anesthetized with isoflurane (1%; n=6), 4 groups of Long Evans rats anesthetized with isoflurane (1%; n=6), Urethane (n=7), Medetomidine (bolus of 0.24 mg/kg and infusion of 0.12 mg/kg/h; n=6), and Etomidate (bolus of 10 mg/kg and infusion, n=7).

Data acquisition: Rats were imaged at 9.4T with a volume transmit, 4-channel surface receive cross coil configuration (Paravision 6.0.1, Bruker, Ettlingen, Germany). After an anatomical T2w scan, cerebral blood flow (CBF) was mapped using pseudo continuous arterial spin labeling (pCASL) following inter-pulse phase optimization (Hirschler et al early view). Then, resting stage fMRI was performed: single shot echo-planar imaging was performed (TE=20 ms, TR=500 ms, spatial resolution 0.47x0.47x1.00 mm, 9 slices, 3600 repetitions, duration: 30min). Eventually, a second CBF map was acquired. Heart rate and breath rates were monitored throughout the entire procedure.

Data processing: Statistical Parametric Mapping program (SPM12, see 1) was used to co-register anatomical, perfusion, and functional MRI data. Perfusion maps were obtained using homemade routines based on 2. CBF values and rs-fMRI time courses were obtained for each of the 51 parcels of an homemade rat brain atlas. Briefly, the atlas was obtained by fusing two existing atlases proposed in 3-4, and merging small regions. Mean CBF values were obtained by averaging the values obtained before and after the rs-fMRI acquisition. Each rs-fMRI time course was decomposed using a dyadic wavelet transform at different scales (s1 to s7, with s4 corresponding to 0.05-0.10 Hz bandwith) with one detail coefficient (d7) that captured the polynomial trends contained in the signal. Standard deviations (std) of the wavelet coefficients in all areas are computed for each area and each individual in each group.

Results

The type of anesthetic modulates the CBF by up to one order of magnitude (Figure 1). For each anesthetic, the CBF values are homogeneous. Moreover, there is no evidence of a link between CBF and physiological components (breath rate, heart rate...) (Figure 2). Figure 3 shows the means and std per bin of 10 ml/ 100 mg / min of the BOLD std per area, for each wavelet coefficients, as a function of CBF. Distribution shapes seem comparable between scales and groups. Generally, the BOLD signals follow a trapezoidal shape with a plateau for CBF valeurs between 20 and 150 ml / 100 g / min, and become null for higher CBF values. In the comparison figure given for s4, the amplitude of the plateaus are very similar, despite the broad range of CBF values. The shapes for Iso-L and Iso-W are slightly different with larger transitions to and from plateau leading to a larger trapezoidal shape. For Iso-W, the BOLD values plateau above 80 ml / 100 g / min and decrease for CBF values above 150 ml / 100 g / min.

Discussion

For a large majority of anaesthetic agents, the amplitudes of the standard deviations of the resting state BOLD signals are not related to perfusion values. When applying wavelets, the amplitudes of

BOLD signals remain large. Wavelets have been shown to handle properly fractal properties of the BOLD signal as reported in 5, which is of particularly interest in the context of brain connectivity.
It is shown here that wavelet decompositions are not altering the BOLD standard deviation, especially at low frequencies usually used for preprocessing BOLD signal as in 5. If all anesthetics show a trapezoidal shapes of distributions with more or less transition steps, isoflurane seems to induced some relations with perfusion, especially for the Wistar strain. This is potentially due to the vasodilator effect of this molecule as noted in 6. Above a certain perfusion level, BOLD fluctuations become null.

Conclusion

For the anaesthetic agents evaluated in this study, dynamics of brain area signals are not related to perfusion values. However, isoflurane yields to reduced or even null BOLD signal, in case of low or of high perfusion, in certain brain areas.

References

1 Members and collaborators of the Wellcome Trust Centre for Neuroimaging, SPM: Statistical parametric mapping, http://www.fil.ion.ucl.ac.uk/spm/
2 Alsop et al 2015
3 P. A. Valdés-Hernandez et al., An in vivo MRI template set for morphometry, tissue segmentation and fMRI localization in rats, Frontiers in Neuroinformatics, 5(26):1-19, 2011.
4 E. A. Papp et al., Waxholm Space atlas of the Sprague Dawley rat brain, Neuroimage, 97: 374-386, 2014.
5 S. Achard et al., A resilient, low-frequency, small-world human brain functional network with highly connected association cortical hubs, J. Neurosci., 26(1): 63-72, 2006.
6 K. S. Hendrich et al., Cerebral perfusion during anesthesia with fentanyl, isoflurane, or pentobarbital in normal rats studied by arterial spin-labeled MRI, Mag. Res. in Med., 46(1): 202-206, 2001.

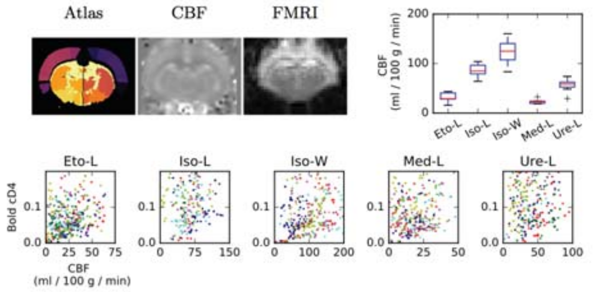

Figure 1: Brain areas of the atlas (atlas), normalized perfusion map (CBF) and normalized FMRI (FMRI). CBF values are computed for each area. CBF distributions per group represented by boxplots for all areas and all individuals. Distributions of the standard deviation values of the wavelet detail coefficients cD4 ([0.06, 0.13[Hz) obtained from the bold signal in each area (Bold cD4) versus CBF. Each color represents an individual inside a group.

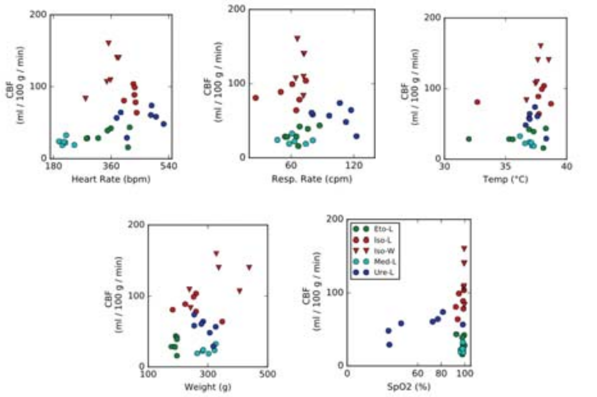

Figure 2: Mean cerebral perfusions (CBF) versus mean physiological values for each individual in each group.

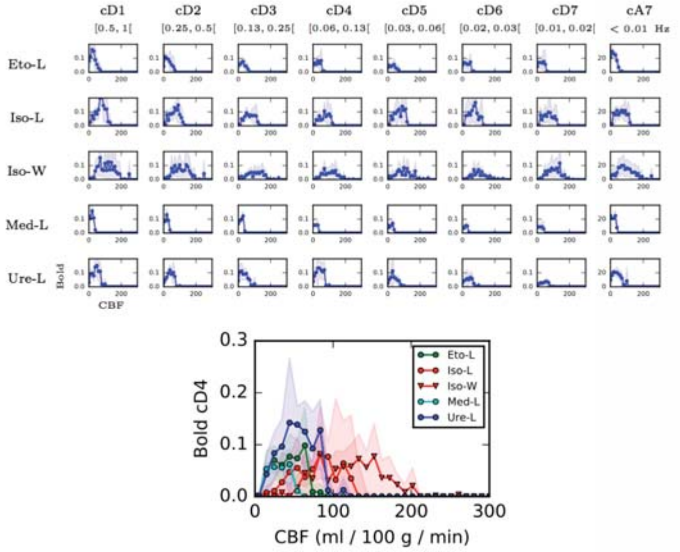

Figure 3: Bold values versus CBF. Means of standard deviations in areas for wavelet details (cD1 - cD7) and approximation (cA7) coefficients. Means are computed per bins of 10 ml / 100 mg / min. A comparison of groups is given for Bold cD4.

Long distance plasticity of callosal connections: From men to mice

Authors: Diego Szczupak[1,2], Cirong Liu[2], Cecil C.C. Yen[2], Fernanda Guimaraes Meireles Ferreira[3], Caroline Victorino de Lima[3], Roberto Lent[1,3], Afonso C. Silva[2], Fernanda Tovar-Moll[1,3]

Affiliations: 1 – Federal University of Rio de Janeiro 2 – National Institutes of Health 3 – Institute D'or Research and Education

Purpose: Brain plasticity is usually associated with microstructural changes, but it can also reflect a large macroscopic rewiring of the brain called long-distance plasticity (LDP). LDP was first described in humans with dysgenesis of the corpus callosum (dCC), a brain malformation in which some or all callosal fibers fail to find their natural tracts and end up forming completely new paths[1]. So far, little is known about the detailed anatomical and temporal pattern of the development of those connections and, to date, no animal model could reproduce the full complexity of brain connectivity in this pathology. In the present study, we used ultra-high field diffusion-weighted MRI to map the underlying formation of white-matter fiber tracts in a long-known murine model of dCC, the Balb/c mouse.

Methods: 81 Balb/c mice were scanned *in vivo* in a diagnostic sequence in a Varian 7T scanner with the following parameters: TR/TE 2500:27 ms; matrix 128 x 128; FOV 23 x 23 mm; slice thickness: 0,25mm; no gap; 8 averages in sagittal plane. The CC area was measured in Balb/c and C57bl6 data[2] on the midline on imageJ program using a freehand drawing tool.Eight adult Balb/c mice (4 females and 4 males) were scanned for DWI following preparation[2] in a 14T vertical bore Bruker with a 15mm coil 3-D spin-echo EPI images were acquired using the following parameters: TR/TE = 450/21ms, δ/Δ = 3/7.5 ms, field of view = 12.80 x 10.24 x 6.40 mm^3, matrix = 160 x 128 x 80 yielding an isotropic resolution of 80μm, averages = 2, 232 directions split in three shells of 39, 77 and 116 directions, b-values = 1500, 3000, 6000 s/mm^2 with 4 b0 images. For probabilistic tractography on mrtrix, ROIs were manually drawn in both hemispheres at the frontal portion of the corpus callosum (CC) (or at the frontal portion of the Probst bundle in case of dCC), the posterior portion of the cortex at the level of mid hippocampus, at the entire CC (or remnant in case of dCC) and at the hippocampal commissure (HC).

Results: In the cohort of 81 animals, we detected a larger variance of the CC of Balb/c (Fig. 1A) compared to C57bl6 data[2]. To better understand these findings, we investigated the whole callosal network of 8 animals. For this, we utilized diffusion-weighted MRI and tractography driven by manually-drawn ROI seeds in the corpus callosum (or the callosal remnant in dCC animals). We found that 4/8 animals presented abnormalities of the CC in an anatomical (b0) image, and that all 8 animals showed abnormalities in the DWI scans. Examples of these abnormalities can be seen in the connectivity of the interhemispheric network, which shows one animal with apparently normotypic cortico-cortical connections (Fig. 1B), together with another animal that presented only a "narrow bridge" juxtaposed to the HC (Fig. 1C). Figure 1 also shows altered frontal interhemispheric connections of the Balb/c mouse. In one animal, this connection crosses the midline through the genu (Fig. 1D), while in another, the frontal fibers continue in an anteroposterior orientation and only cross the callosal remnant at the HC level (Fig. 1E). Another anomalous connectivity found in these mice (Figs. 1F and G) was the sigmoid bundle, an anomalous heterotopic bundle that connects the frontal cortex with posterior contralateral cortex, and which has been thus far only described in humans [1].

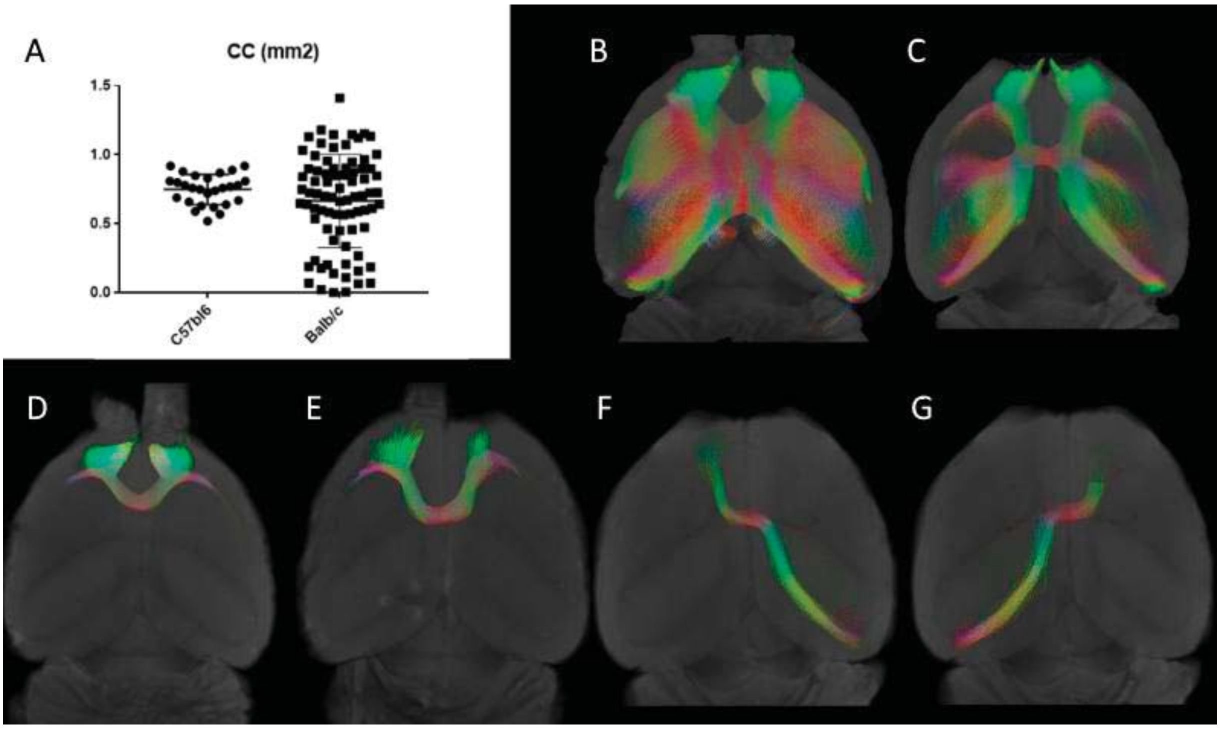

Figure 1. A. Graph showing the greater variability of the size of the CC in Balb/c as compared with controls, in sagittal view. **B-G**. Tractography of the global callosal network: frontal connectivity of a Balb/c mouse with a normal sized CC (**B** and **D**) compared to a dCC mouse (**C** and **E**). **F** and **G**. Tractography of the sigmoid bundles of a dCC animal.

Conclusion: Diffusion-weighted MRI allowed to observe, in the Balb/c strain, some of the aberrant connections seen in humans with dCC. This set of results allows us to reinforce previous proposals[4] to consider the Balb/c strain as an appropriate translational animal model to study LDP. Using this model, it may be possible to perform detailed investigations of the genetic and molecular underlying mechanisms of aberrant white-matter tract formation in the brain, and to combine developmental studies with morphological and functional imaging approaches aimed at understanding and mitigating the consequences dCC in human patients.

References

1. Tovar-Moll F, Monteiro M, Andrade J, et al. Structural and functional brain rewiring clarifies preserved interhemispheric transfer in humans born without the corpus callosum. Proc Natl Acad Sci. 2014;111:7843–7848.
2. Liu C, Li Y, Edwards T et al. Altered structural connectome in adolescent socially isolated mice. NeuroImage. 2016;139:259-270.
3. Andersson, JLR and Sotiropoulos SN. An integrated approach to correction for off-resonance effects and subject movement in diffusion MR imaging. NeuroImage.2016;125:1063-1078.
4. Livy DJ, Wahlsten D. Retarded formation of the hippocampal commissure in embryos from mouse strains lacking a corpus callosum. Hippocampus. 199;7;2–14.

fMRI Visual Responses of a Rat Model of Parkinson's Disease

Emmanuelle Bellot[1], Arnaud Pautrat[1], Nora Collomb[2], Olivier Montignon[2], Véronique Coizet[1], Michel Dojat[1]

[1] Univ. Grenoble Alpes, Inserm, CHU Grenoble Alpes, GIN, 38000 Grenoble, France
[2] Cnrs, Inserm, CHU Grenoble Alpes, IRMAGE, 38000 Grenoble, France

<u>Introduction.</u> Parkinson's disease (PD) is a neurodegenerative disorder characterized by the progressive loss of dopaminergic neurons. Sensory disorders are associated with PD and appear a long time before the onset of the well-known motor symptoms. A recent electrophysiological study in a PD rat model [1] has revealed the dysfunction of the Superior Colliculus (SC), a retinotopic structure of the midbrain involved in vision [2]. We explored with fMRI the response to light stimulus frequency of primary visual structures (SC, lateral geniculate nucleus LGN, and primary cortical area V1) in a rat model of PD. Activation of SC was exacerbated at low frequency (0.5-5%) and rapidly saturated compared to controls. These results confirm the possible role of SC as an early biomarker of the disease.

<u>Methods</u>. *Animals*. Eight Long Evans (LG) rats (Controls) and six parkinson rat (PD) models (LG with an intracerebral injection of 6-hydroxydopamine) were anesthetized with a intramuscular injection of Medetomidine 0.5ml/kg (Domitor, Pfizer). There were no difference in age and weight between the two groups (6±1 weeks, 320g±12). Rats were spontaneously breathing throughout the entire experiment. Breathing rate and SaO_2 were monitored using BioPac and MouseOx systems respectively. Body temperature was monitored with a rectal probe and maintained in the normal range using a heated blanket. All procedures were approved by a local ethical review committee. Before a second imaging session, PD treatment (LDopa, 0.1ml/kg) was administred to both groups.

MRI. All the images were acquired using a 9.4 T horizontal scanner (Brüker). Radiofrequency (RF) transmission was done with a Helmholtz coil (diam: 50 mm). A circular receiver surface coil (diam: 24 mm) was placed above the dorsocaudal part of the brain. Functional images consisted in a T2*-weighted sequence (TE/TR/flip angle=20 ms/2s/90°, matrix size=64 x 64, FOV=30x30mm, in-plane resolution=0.469 x 0.469 mm^2 , slice thickness=1 mm). The T2-weighted Turbo Rare structural image comprised fifty coronal slices (TE/TR/flip angle=36ms/5.7s/90°, echo-spacing=8ms, Rare factor=8, average=6, matrix size= 256 x 256, FOV=30x30, in-plane resolution=0.117 x 0.117 mm^2, slice thickness=0.5 mm).

Stimulus and visual stimulation. To modulate the functional SC activity the block visual paradigm consisted in monocular 5ms light flashes emitted by a blue LED (450 nm, 100cd/m^2). Each fMRI run was composed of 10 stimulation blocks, 12s each, alternating with a 20s rest period. In each block the light stimulus frequency was kept constant. Five different frequencies were used 1Hz, 3hz, 5Hz, 8Hz and 10Hz in a first experiment (Exp1, 4 controls and 4 PD) and 0.5Hz, 1Hz, 2hz, 3Hz and 5Hz in a second experiment (Exp2, 4 controls and 2 PD). Frequencies were randomly presented in 14 fMRI separate runs for each animal leading to 28 events of each frequency type. A jitter was introduced to avoid synchronization between image acquisition and visual stimulation. All aspects of stimulus delivery were controlled via an home-made software controller. The monocular visual stimulation was transmitted via an optic fiber to the left eye of the rat.

Data Analysis. All data were processed using SPM12 (http://www.fil.ion.ucl.ac.uk/spm). As SPM was initially developed for Human, the images were firstly rescaled by a 10 multiplicative factor. Then, functional images were realigned (rigid body transformation) to correct for possible head movements to the first image acquired after the structural image used as the reference and a mean functional volume was computed. After realignment to the functional mean, the structural image was non-linearly deformed to fit an home-made atlas. The computed individual deformation field was applied to all corresponding functional images. Individual functional images were analysed separately using a General Linear Model. The six conditions of interest (5 frequencies and rest) were modeled as six regressors constructed as a boxcar function convolved with a canonical response function. To specifically study the involvement of the first steps of visual information processing, we conducted a region-of-interest (ROI) analysis in SC, LGN and V1, defined based on our atlas. Contrast images were computed based on the GLM relative to each stimulus condition compared to the baseline (rest) across all experimental runs. For each ROI (SC, LGN and V1) we retained voxels that showed a significant t-value (p<0.05 family wise error (FWE) corrected). For each subject voxels of contrast images were averaged in each ROI.

Results. Following the retinotopic property of the first steps of the visual pathway, a monocular left visual stimulation led to BOLD activation in the contralateral hemisphere and few contralateral activation. In Exp1., ROI activation was higher for the control group compared to the PD group. The most sensitive regions were SC and LGN: 46% and 88% of their voxels were respectively activated in controls vs 33% and 46% in PDs. As shown in Figure 1, the SC response was linearly modulated by light stimulus frequency with a saturation at 8Hz for controls. For PDs, the SC response was sharper and more rapidly saturated (5Hz). This was confirmed when light frequency varied between 0.5-5Hz (Exp2). SC response seemed exacerbated in PD compared to controls (Figure 2). Similarly to [3] we noted that BOLD signal was attenuated in the cortex compared to subcortex. The effect of dopaminergique was weak.

Discussion. This work represents the first fMRI study of frequency dependence in the visual pathway of PD rat model. On controls it complements the work of [3, 5] on SC activity in response to changes in light frequency. This response is linear in the 1-10Hz range in normal conditions. With PD, the SC response is enhanced and rapidly saturated. This may reflects the overcompensation to combat the inhibition exerted by the degeneration of the dopaminergic neurons of the Substancia Negra reticulata. The dopaminergic treatment (bolus) seems not to restore the SC function. This results confirm the possible role of SC as an early biomarker of the disease [4]. More data are required to confirm these preliminary results.

Acknowlegments. E. Bellot is recipient of a grant from the France Parkinson foundation and from the Université Grenoble Alpes. A. Pautrat is financially supported by a grant from the Auvergne-Rhône-Alpes region. This work was partly supported by a grant from 'La Fondation de l'Avenir' (France). The Grenoble MRI facility IRMaGe was partly funded by the French program 'Investissement d'Avenir' run by the Agence Nationale pour la Recherche (ANR-11-INBS-0006).

References

1. Rolland M et al. Neuroscience. 2013;252:277-88.
2. Schneider KA et al. J Neurophysiol. 2005;94(4):2491-503.
3. Pawela CP et al. Neuroimage. 2008;41(2):525-34.
4. Bellot E et al. International Congress of Parkinson's Disease and Movement Disorders; (Ca) 2017.
5. Van Camp N et al. BOLD fMRI. J Neurophysiol. 2006;95(5):3164-70.
6. Lau C et al. Neuroimage. 2011;58(3):878-84.

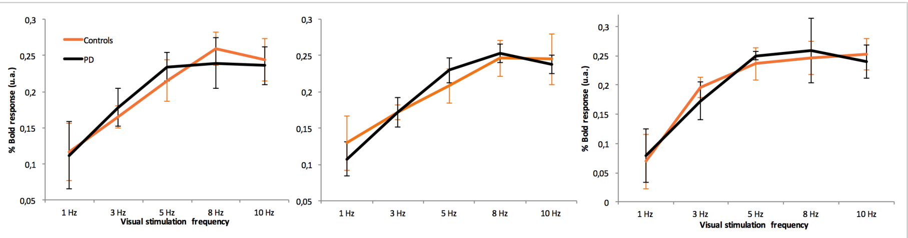

Figure 1: Modulation of BOLD response function of the visual stimulation frequency in superior SC (left), deep SC (middle) and LGN (right). Mean on 4 rats, vertical bar: standard error, a.u.: arbitrary unit, activated voxels p<0.05 FWE corrected.

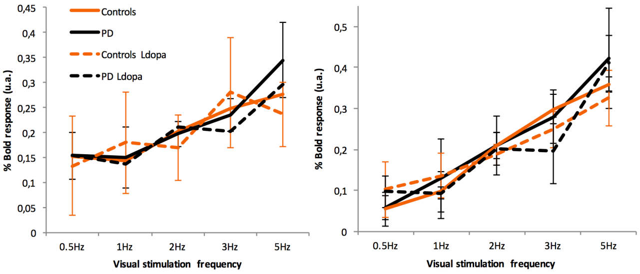

Figure 2: Modulation of BOLD response function of the visual stimulation frequency in superior SC (left), and LGN (right) without and with Ldopa treatment. Mean on 4 rats (controls) and 2 rats (PD), vertical bar: standard error, a.u.: arbitrary unit, activated voxels p<0.05 FWE corrected.

Monitoring glioma heterogeneity during tumor growth using clustering analysis of multiparametric MRI data

Benjamin Lemasson[1,2], Nora Colomb[1,2], Alexis Arnaud[3], Florence Forbes [3] and Emmanuel L. Barbier[1,2]

[1]U1216, Inserm ; [2]Grenoble Institut des Neurosciences (GIN) and [3]MISTIS (INRIA Grenoble Rhône-Alpes / LJK Laboratoire Jean Kuntzmann)

Introduction: For tumor diagnosis, histology often remains the reference, but due to tumor heterogeneity, it is widely acknowledged that biopsies are not reliable. There is thus a strong interest in monitoring quantitatively intralesional brain tumor heterogeneity. MRI has demonstrated its ability to quantitatively map structural information like diffusion (ADC) as well as functional characteristics such as the blood volume (BVf), vessel size (VSI), the oxygen saturation of the tissue (StO2), or the blood brain barrier permeability. In a recent study (1), these MR parameters were analyzed independently from each other to demonstrate the great potential of a multiparametric MR (mpMRI) protocol to monitor combined radio- and chemo-therapies. However, to summarize and quantify all the information contained in an mpMRI protocol while preserving information about tumor heterogeneity, new methods to extract information need to be developed. The goal of this study is to demonstrate the ability of clustering analysis (2) applied to longitudinal mpMRI to summarize and quantify intralesional heterogeneity during tumor growth.

Methods: Animal model: The local IRB committee approved all studies. 9L tumors were implanted in 8 rats and imaging was performed every 2 days between day 7 and day 17 post tumor implantation on a 4.7T Bruker system (D7, D9, D11, D13, D15 and D17; respectively). The following mpMRI protocol was acquired at each MR session: a T2-weighted spin echo sequence to obtain structural information over the whole brain, a diffusion weighted EPI sequence to map the Apparent Diffusion Coefficient (ADC) and multiple spin/gradient echo sequences to map T2 and T2*. A Gradient Echo Sampling of the FID and Spin Echo (GESFIDE) sequence was acquired pre- and post-injection of USPIO (133 µmol/kg). A dynamic contrast enhancing sequence was acquired using a RARE sequence (T1w images; n=15, 15.6 sec per image). After the acquisition of 4 images, a bolus of gadolinium-chelate was administered (100µmol/kg). Parametric maps: for each MR session, BVf and VSI maps were computed using the approach described in (3), StO2 using the method described in (4) and the vessel permeability maps (Perm) was calculated as the percentage of enhancement (voxel-wise) within 3 min post injection of gadolinium (cf. fig1-a). Co-registration: each parametric map of each MR session was co-registered to that acquired at the previous time point using rigid registration (SPM toolbox and Matlab). ROI: tumor was manually delineated using the T2w images (Tumor-ROI; Red line in fig 1-a). Cluster analysis: parameter values were centered and normalized. Then, a Gaussian mixture distribution (Matlab function called: fitgmdist) was use to performed the clustering analysis of all voxels included in the tumor-ROI. The number of classes inside the mixture was selected by minimizing the Bayesian information criterion (BIC).

Results: Firstly, we performed the clustering analysis 9 times using 1 to 9 classes. The optimal classes number, defined by the BIC was 5. Each cluster may be seen as a tissue type, as described Fig.1-E. The result of the clustering analysis is illustrated Fig1-A for one animal. For each of the five clusters (labeled K1 to K5), the evolution of the mean cluster volume over the entire population of tumor is presented Fig 1-B. Note that the sum of the five cluster volumes represents the whole tumor volume. Fig.1-C illustrates the longitudinal evolution of the 5 clusters in 2 animals with different tumor growth rate (slow on the top and high on the bottom). Although the cluster analysis analyzed every voxel independently from each other, one can see that the clustering results are spatially consistent at 1 time point but also over time. Indeed, clusters are spatially grouped: for example, the green cluster is mostly located in the center of the tumor (Fig1-C). Our result shows a difference in cluster composition between the slow and the high growth rate tumors (Fig.1-C, D). For example, in the slow growth rate tumor, the yellow cluster takes more and more space in the tumor overtime (up to 49% at D17) whereas, in the high growth rate tumor, it is the green one. The main difference between the yellow and the green cluster is the strong reduction in StO2 in the green cluster versus the yellow cluster (cf. Fig.1-E).

Conclusions: To our knowledge, it is a first study demonstrating the feasibility of performing a clustering analysis on mpMRI data to monitor the evolution of brain tumor heterogeneity in vivo. This approach highlights the type of tissue, which mostly contributes to the development of the tumor. The composition in tissue type could be used to refine the evaluation of chemo and radiotherapies and could contribute to improve tumor prognosis.

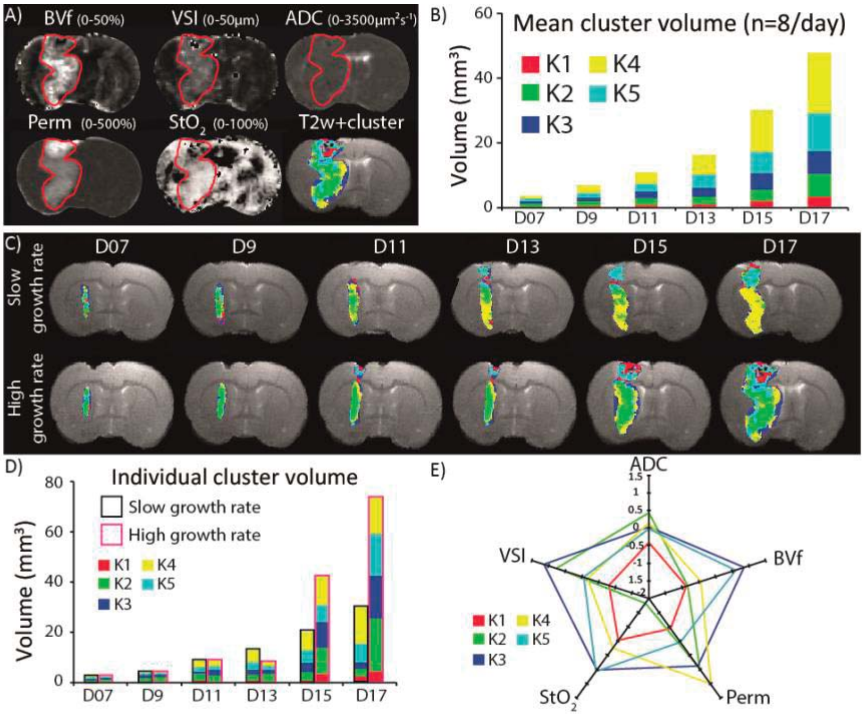

Figure1: A) Representative images of one animal acquired 17 days post tumor inoculation. The red line corresponds to the manual tumor delineation. Color-coded clustering result is overlaid on T2w image. B) Histogram of the mean cluster volume across all animals measured at each time point. C) Color-coded clustering results overlaid on the T2w image of 2 animals: a slow and a high growth rate. D) Histogram of the cluster volume at each time point for the slow and high growth rat animals presented. E) Description of each cluster across each MR parameters.

References:

1. Lemasson B, Bouchet A, Maisin C, Christen T, Le Duc G, Remy C, et al. Multiparametric MRI as an early biomarker of individual therapy effects during concomitant treatment of brain tumours. NMR Biomed. 2015;28(9):1163-73. Epub 2015/08/01.
2. Coquery N, Francois O, Lemasson B, Debacker C, Farion R, Remy C, et al. Microvascular MRI and unsupervised clustering yields histology-resembling images in two rat models of glioma. J Cereb Blood Flow Metab. 2014;34(8):1354-62. Epub 2014/05/23.
3. Tropres I, Grimault S, Vaeth A, Grillon E, Julien C, Payen JF, et al. Vessel size imaging. Magn Reson Med. 2001;45(3):397-408.
4. Christen T, Lemasson B, Pannetier N, Farion R, Segebarth C, Remy C, et al. Evaluation of a quantitative blood oxygenation level-dependent (qBOLD) approach to map local blood oxygen saturation. NMR Biomed. 2011;24(4):393-403. Epub 2010/10/21.

Using Imaging to Better Understand the Genetic Control of Brain Circuit Vulnerability in Mouse Models of Alzheimer's Disease

Alexandra Badea[1], Michele Wang[1], Robert J Anderson[1], Yi Qi[1], Gary Cofer[1], Nian Wang[1], G Allan Johnson[1], Shangsi Wang[2], Joshua T. Vogelstein[3,4], Carey E. Priebe[2,3], Joan Wilson[5], Carol Colton[5]

1. Center for In Vivo Microscopy, Department of Radiology, Duke University Medical Center, USA
2. Department of Applied Mathematics and Statistics, Johns Hopkins University, USA
3. Center for Imaging Science, Johns Hopkins University, USA
4. Department of Biomedical Engineering and Institute for Computational Medicine, Johns Hopkins University, USA
5. Neurology Department, Duke University Medical Center, USA

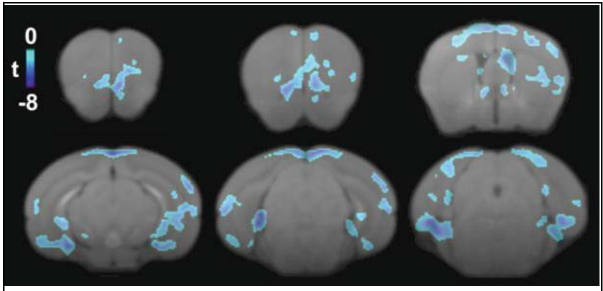

Fig 1. *In vivo* voxel-wise statistics show reduced volume in the entorhinal cortex of APOE4/HN mice relative to APOE3/HN controls (cluster level p<0.05, FDR corrected, at 5%).

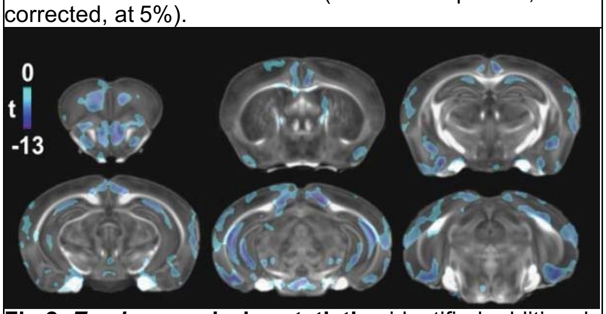

Fig 2. *Ex vivo* voxel wise statistics identified additional areas of atrophy in APOE4HN mice relative to APOE3/HN controls including hippocampus and amygdala (cluster level p<0.05, FDR corrected at 5%).

Introduction. MRI can detect early brain atrophy in aging normal populations [1] and AD patients [2], and these changes do not affect the brain uniformly. Vulnerable circuits include the hippocampus and entorhinal cortex and the white matter tracts connecting them[3,4]. Moreover, microstructural changes involving gray and white matter are found in aging and AD using Diffusion Tensor Imaging (DTI)[5,6]. We use MRI as a translational tool to determine image based signatures in huAPOE- huNOS2 mouse models, which better replicate the human immune response, an important predictor of brain aging [7]. To help reveal the APOE associated basis for brain circuit vulnerability we have used male and female APOE4/HN models of high genetic risk for Alzheimer's disease, and APOE3/HN controls, aged to 12-13 months, because these animals more accurately model the human aging and immune environment[8,9].

Methods. Using in vivo MRI at 7.1 T we measured in a physiological milieu regional brain volumes, as surrogates of neuronal numbers. At the end of in vivo experiments, mice were sacrificed and imaged at 9.4T with diffusion tensor imaging (DTI) to derive microstructural and connectivity information. The resulting tractography was used to evaluate network wide distributed changes with APOE-genotype. We hypothesize that genotype, modulates imaging and network properties, in particular in vulnerable circuits. We focused on the hippocampus, entorhinal cortex and amygdala as vulnerable regions, respectively. To explore the relationship with learning and memory mice were tested in the Morris Water Maze using a 5 days paradigm. We examined the correlation between cognitive and imaging/connectome markers.

Results. 13 months old APOE3/HN and APOE4/HN mice present significant differences in total brain volume, larger in APOE3/HN (522.44±17.52 mm^3) relative to APOE4/HN mice (488.64±11.21 mm^3), $p=8*10^{-6}$. Differences are localized to brain areas, including the entorhinal, temporal association and cingulate cortices (FDR<0.05) (**Fig 1**).

Manganese enhanced MR images acquired *in vivo* at 100 μm resolution, detected areas with significant atrophy in APOE4/HN mice relative to APOE3/HN controls. These areas affected the olfactory, cingulate and entorhinal cortices, as well as the hippocampus. Our preliminary data support that the manganese enhanced contrast increases the accuracy of segmentation and voxel based morphometry so that changes in volume were detected at a level of 0.1 FDR correction in unstained CVN brains, but improved to the 0.05 level in Mn contrast enhanced brains. *In vivo* Mn enhanced MRI detected significant hippocampal and cortical atrophy in APOE4/HN relative to APOE3/HN mice, notably in the cingulate, entorhinal and temporal association cortices (**Fig 2**). To increase sensitivity and resolution, we used *ex vivo* imaging of fixed specimens prepared with Gd (gadolinium) staining through transcardiac perfusion, and imaged at 55 µm **resolution, and detected** additional areas of atrophy including the amygdala, hypothalamus and substantia nigra (**Fig 2**).

We have also developed methods for structural connectomics[10]. Our protocol uses compressed sensing diffusion tensor imaging (DTI with 51 diffusion directions, allowing for efficient sampling, and reconstruction of white matter tracts through the whole brain with good accuracy. The number of tracts connecting each pair of atlas regions is used to build connectomes, that can be statistically analyzed to reveal network changes.

Our data suggest that subgraphs of ~30 vertices (10 are shown in **Fig 3**) may account for the differences between the network characteristics of APOE3/HN and APOE4/HN mouse brains. These networks include the entorhinal cortex, amygdala, presubiculum, hippocampus, and septum. We found significant correlations between behavioral metrics (e.g. swim distance) and graph properties (e.g. centrality) for the entorhinal cortex (R=- 0.4, p=0.003), hippocampus (R=-0.5, p=0.006), and amygdala (R=-0.4, p=0.007). [11]

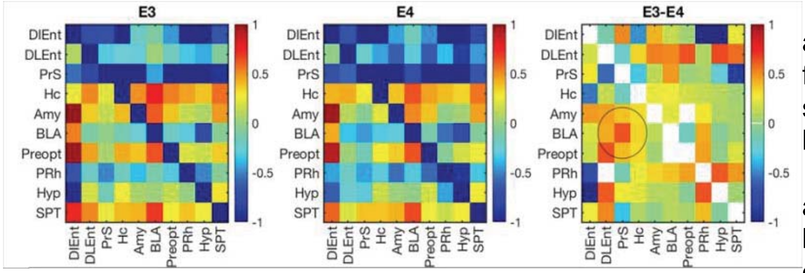

Fig 4. APOE alleles modulate connectivity in particular in vulnerable circuits connecting the entorhinal cortex (Ent), hippocampus (Hc), and amygdala (Amy) (circle). where APOE3/HN mice had higher connectivity relative to APOE4/HN mice.

Conclusion. We identified behavioral, and imaging signatures consistent with features of human Alzheimer's disease, in similar vulnerable circuits. Relative to human clinical populations with complex genetics and environmental exposure, animal models have uniform genetic backgrounds, and are raised in uniform environments. High resolution population imaging in small animal models can help better understand the genotype influences on brain circuit vulnerability, to offer novel insight and models for how APOE modulates the aging process and acts to confer increased AD risk.

References

1. Abe O, Yamasue H, Aoki S, et al. Aging in the CNS: comparison of gray/white matter volume and diffusion tensor data. *Neurobiol Aging.* 2008;29(1):102-116.
2. Jack Jr CR, Petersen RC, Xu YC, et al. Prediction of AD with MRI-based hippocampal volume in mild cognitive impairment. *Neurology.* 1999;52(7):1397- 1403.
3. Jack CR, Jr., Petersen RC, Xu YC, et al. Medial temporal atrophy on MRI in normal aging and very mild Alzheimer's disease. *Neurology.* 1997;49(3):786-794.
4. Eskildsen SF, Coupe P, Fonov VS, Pruessner JC, Collins DL. Structural imaging biomarkers of Alzheimer's disease: predicting disease progression. *Neurobiol Aging.* 2015;36 Suppl 1:S23-31.
5. Bozzali M, Falini A, Franceschi M, et al. White matter damage in Alzheimer's disease assessed in vivo using diffusion tensor magnetic resonance imaging. *J Neurol Neurosurg Psychiatry.* 2002;72(6):742-746.
6. Ihara M, Polvikoski TM, Hall R, et al. Quantification of myelin loss in frontal lobe white matter in vascular dementia, Alzheimer's disease, and dementia with Lewy bodies. *Acta Neuropathol.* 2010;119(5):579-589.
7. Corlier F, Hafzalla G, Faskowitz J, et al. Systemic inflammation as a predictor of brain aging: Contributions of physical activity, metabolic risk, and genetic risk. *Neuroimage.* 2018;172:118-129.
8. Vitek MP, Brown CM, Colton CA. APOE genotype-specific differences in the innate immune response. *Neurobiol Aging.* 2009;30(9):1350-1360.
9. Hoos MD, Vitek MP, Ridnour LA, et al. The impact of human and mouse differences in NOS2 gene expression on the brain's redox and immune environment. *Mol Neurodegener.* 2014;9:50.
10. Calabrese E, Badea A, Cofer G, Qi Y, Johnson GA. A Diffusion MRI Tractography Connectome of the Mouse Brain and Comparison with Neuronal Tracer Data. *Cereb Cortex.* 2015;25(11):4628-4637.
11. Badea A, Kane L, Anderson RJ, et al. The fornix provides multiple biomarkers to characterize circuit disruption in a mouse model of Alzheimer's disease. *Neuroimage.* 2016;142:498-511.

Neuroimaging in an Autism Related Mouse Population

Jacob ELLEGOOD[1], R. Mark HENKELMAN[1,2], Jason P. LERCH[1,2]

1. Mouse Imaging Centre, Hospital for Sick Children, Toronto, Ontario, Canada
2. Department of Medical Biophysics, University of Toronto, Toronto, Ontario, Canada

Introduction – Autism is characterized by two distinct behavioural domains: 1) Deficits in social communication and interaction, and 2) repetitive behaviours and restricted interests (DSM V APA ref). Autism is extremely heterogeneous, with marked behavioural, genetic, and neuroanatomical heterogeneity found across the population. As of February 2018, the Simon's Foundation Autism Research Initiative (SFARI) gene database lists 990 genes that have been linked to autism [1, 2]. Of those 990 genes, 267 different mouse models have been created with mutations in those genes. Over the past ten years, using the high throughput techniques pioneered by the Mouse Imaging Centre (MICe) [3], and in an effort to characterize and contrast the neuroanatomical differences across the autism related mouse population [4], we have created an neuroimaging dataset of 101 different mouselines related to autism. This dataset of 3740 mice has allowed us to examine both the heterogeneity of autism in the mouse as well as link several of the imaging findings to what has been shown in the human population.

Material and Methods – A multi-channel 7.0 Tesla MRI was used to acquire anatomical images of the ex vivo mouse brain, which is left in the skull, after perfusion and fixation. During the last 10 years we have had several sequence and scanner hardware upgrades, so the sequence has evolved over time to become more efficient and increase our isotropic resolution. The current sequence is a T2 weighted 3D fast spin echo (FSE) sequence, with a cylindrical acquisition of k-space, and with a TR of 350 ms, and TEs of 12 ms per echo for 6 echoes, two averages, filed-of-view of 20 x 20 x 25 mm^3 and a matrix size of 504 x 504 x 630 giving an image with 0.040 mm isotropic voxels [5]. The current scan time of this sequence is ~14 hours and 16 brains are scanned in parallel during one session. To visualize and compare any differences in the mouse brains, the images from all brains are registered together. All registrations are performed with a combination of mni_autoreg tools [6] and advanced normalization tools (ANTs) [7, 8]. The result of the deformation based registration allows for the analysis of the deformations and how they relate to genotype [9], which can be used to assess the neuroanatomy in different mouselines voxelwise and/or using a pre-existing regional atlas including 199 different regions throughout the brain [10-13].

Results – Figure 1A shows the number of scans of autism related mouse models starting in 2008. Notice the dramatic increase in those scans in the last four years. Figure 1B shows the most affected regions across all the mouse models. Several of these regions including the striatum, hypothalamus, and cerebellum have all been implicated in human autism.

Having this large a population of autism related mouse models has allowed us to start investigating population differences, which has shown a loss of asymmetry across the population (Figure 2), as well as

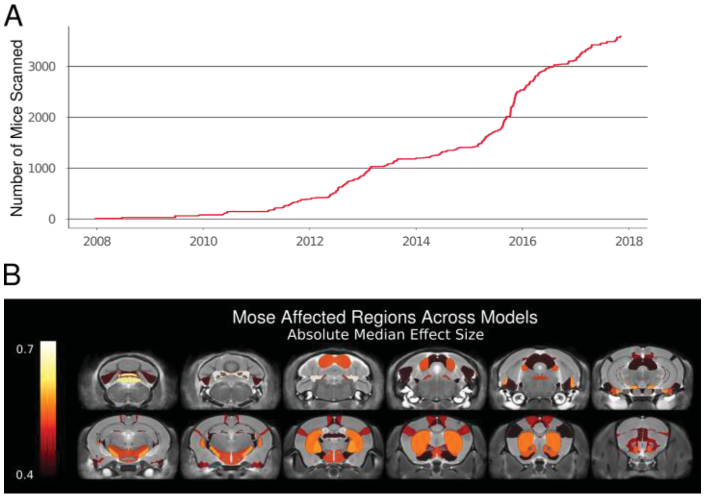

Figure 1 – A) Number of mice scanned from 2008 to 2018. B) Most affected regions across all models measured in absolute median effect size

a modification in the cerebellum to cortex network examined with anatomical covariance (Figure 3).

Of the 131 lateralized regions in our atlas, 53% showed a loss in lateral asymmetry; additionally, as shown in Figure 2, we found a loss in lateral asymmetry in the autism mutants in the 3 largest areas of asymmetry in the mouse brain.

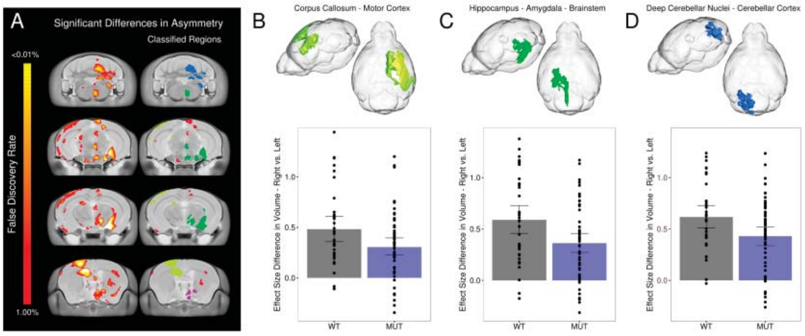

Figure 2 – Significant differences in the effect size between right and left hemispheres in the 3 largest regions of asymmetry in the MUT and WT groups.

The deep cerebellar nuclei (DCN) outputs are one of the most affected regions across the brain (Figure 1B). We examined the projections from the DCN using anatomical covariance to assess the structural connectivity [14]. The covariance was measured between the DCN and the cerebellar cortex, thalamus, pontine nucleus, and the cortex, and was found to be altered only between the DCN and cortex (Figure 3, interaction p=0.01) in the autism models when compared to the WT.

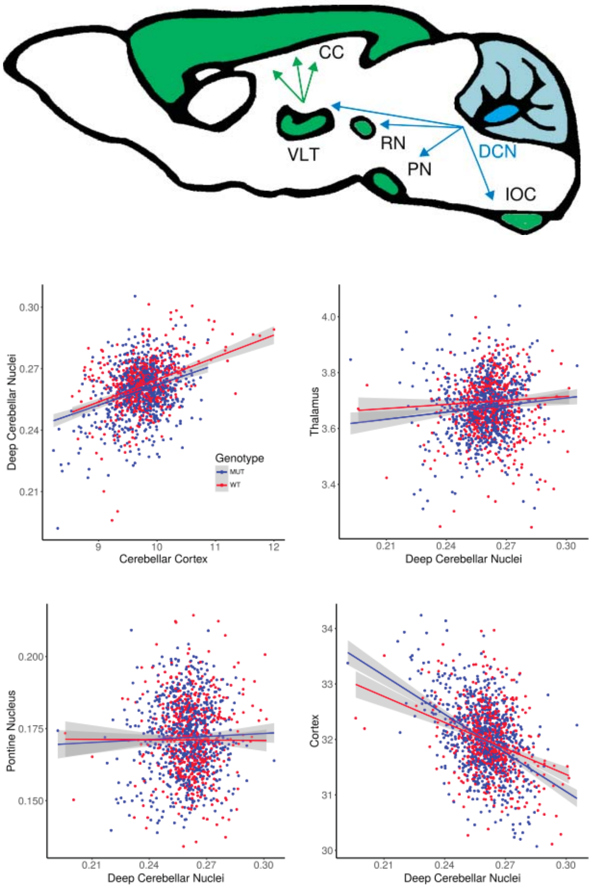

Figure 3 –Schematic of the communication network of the cerebellum particularly the outputs of the DCN. Anatomical covariance networks between the DCN and the Cerebellar Cortex, the Thalamus , the Pontine Nucleus and the Cerebral Cortex.

Discussion/Conclusion – There is never going to be just one mouse model that encompasses all of autism due to the heterogeneity of the disorder. Thus, the only way to truly understand the differences across the human population in a model system is through a genetically heterogenous animal population imaging in order to get a representative sample as heterogeneous as the human population.

What we have shown here has only scratched the surface of what is possible with this large autism related mouse population. We have also released this data publically for the first 30 models, with more to come over time (https://www.braincode.ca/)

References:

1. Banerjee-Basu, S., et al. (2010). Dis Model Mech *3*, 133–135. 2. Basu, S. N., et al. (2009). Nucleic Acids Res. *37*, D832–6. 3. Bock, N. A., et al. (2005). Magn Reson Med *54*, 1311–1316. 4. Ellegood, J., et al. (2014). Mol. Psychiatry. 5. Spencer Noakes, T. L., et al. (2017). NMR Biomed *30*. 6. Collins, D. L., et al. (1994). J Comput Assist Tomogr *18*, 192–205. 7. Avants, B. B., et al. (2008). Med Image Anal *12*, 26–41. 8. Avants, B. B., et al. (2011). Neuroimage *54*, 2033–2044. 9. Lerch, J. P., et al. (2011). Methods Mol. Biol. *711*, 349–361. 10. Dorr, A. E., et al. (2008). Neuroimage *42*, 60–69. 11. Steadman, P. E., et al. (2014). Autism Res *7*, 124–137. 12. Ullmann, J. F. P., et al. (2013). Neuroimage *78*, 196–203. 13. Richards, K., et al. (2011). Neuroimage *58*, 732–740. 14. Evans, A. C. (2013). Neuroimage *80*, 489–504.

Glial and axonal changes in the cuprizone mouse model investigated with diffusion-weighted magnetic resonance spectroscopy

Guglielmo GENOVESE[1-2], Mathieu SANTIN[1-2], Marco PALOMBO[3], Julien VALETTE[4], Clémence LIGNEUL[4], Marie-Stéphane AIGROT[1], Mehdi FELFLI[2], Nasteho ABDOULKADER[2], Dominique LANGUI[1-5], Aymeric MILLECAMPS[1-5], Anne BARON-VAN EVERCOOREN[6-7-8], Bruno STANKOFF[1-8], Stéphane LEHERICY[1-2], Alexandra PETIET[1-2], Francesca BRANZOLI[1-2]

[1]UPMC / INSERM UMR975, Brain and Spine Institute, Paris, France, [2]Center for Neuroimaging Research, Brain and Spine Institute, Paris, France, [3]Department of Computer Science and Centre for Medical Image Computing, University College of London, London, United Kingdom, [4]Molecular Imaging Research Center, CEA, Fontenay-aux-Roses, France, [5]Core Facility ICM.Quant, Brain and Spine Institute, Paris, France, [6]INSERM, U1127, Brain and Spine Institute, Paris, France, [7]Université Pierre et Marie Curie-Paris 6, UMR_S 1127, Paris, France, [8]CNRS, UMR 7225, Paris, France.

Introduction: Diffusion-weighted MR spectroscopy (DW-MRS) is a unique technique to disentangle different pathological mechanism of brain tissue, by providing specific markers of axonal, myelin and glial cells damage[1-2]. In particular, diffusion of N-acetylaspartate + N-acetylglutamate (tNAA) has been suggested as a marker of intra-axonal damage[3], while diffusion of choline compounds (tCho) gives insight onto alterations of glial cells[4]. Here we used the cuprizone (CPZ) mouse model to reproduce pathological features of multiple sclerosis (MS), such as inflammation and demyelination[5]. The aim of this study was to compare the concentrations and apparent diffusion coefficients (ADCs) of the different metabolites measured in CPZ mice with those of healthy control mice, and to correlate these measures with histological changes, in order to determine whether DW-MRS may provide reliable biomarkers of axonal, myelin and glial cells integrity.

Material and Methods: Nine CPZ mice and 10 healthy mice were scanned with an 11.7 T Bruker scanner using a diffusion-weighted STE-LASER sequence[6]. A volume of interest (VOI) of 6x1.5x3 mm^3 was located in the body of the corpus callosum (CC) (Fig .1). Spectra were acquired with TE/TR = 25/5000 ms, and TM = 40 ms. Diffusion weighting was applied in three orthogonal directions with diffusion time $\Delta = 60$ ms and four b-values of 30, 2000, 4000, 6000 s/mm^2 (32 averages per condition) (Fig. 2). Unsuppressed water data were also acquired in the same VOI and with the same diffusion-weighting conditions for eddy current corrections. At each b-value, frequency and phase correction were performed on single scan before averaging, with in-house written routines in Matlab. Spectra quantification was performed with LCModel software. Data were considered reliable and selected according to Cramer-Rao lower bound (CRLB) thresholds (CRLB <5% for tNAA, tCr (creatine + phosphocreatine) Tau (taurine) and Glx (glutamate+glutamine), CRLB <10% for tCho, Ins (inositol)). ADCs were calculated for tNAA, tCho and Ins by log-linear regressions of the signal decay plotted as function of the b value.

Results: Metabolite concentrations were expressed as concentration ratios relative to tCr, since the absolute tCr concentration (calculated with respect to the water reference) did not change significantly between CPZ and healthy mice. Statistically significant variations were observed in tNAA/tCr, tCho/tCr, Tau/tCr and Glx/tCr ratios ($p < 0.005$) (Fig. 3). Interestingly, a statistically significant increase was observed in the ADCs of tCho ($p < 0.005$) and Ins ($p < 0.01$) in CPZ mice compared to healthy mice, whereas no significant variation was found in ADC of tNAA (fig. 4).

Discussion/Conclusion: The measured concentration ratios were in good agreement with previous findings[7]. Decrease of tNAA/tCr ratio in CPZ mice is well in line with demyelination processes confirmed by decreased myelin immunofluorescence. Increase of Tau/tCr ratio likely reflects the presence of inflammation evidence by increased astrocytes and microglia immunofluorescence whereas decrease of Glx/tCr ratio can be correlated to a mitochondrial dysfunction. Decrease of tNAA/tCr concentration ratio in presence of no variation in tNAA ADC could reflect myelin damage but axonal integrity as confirmed by normal neurofilament immunofluorescence and by intact axonal diameters from electron microscopy measures. Increase of tCho and Ins ADCs could be explained by glial cell activation/swelling induced by inflammation processes. In conclusion, these findings suggest new useful DW-MRS biomarkers to highlight specific pathological microstructural alterations of CPZ model. The full study will incorporate correlations between DW-MRS biomarkers and histological data.

References [1] Nicolay et al, NMR Biomed, 14:94-111 (2001).
[2] Ronen and Valette, eMagRes, 4:733-750 (2015).
[3] Wood et al, J Neurosci, 32(19):6665-6669 (2012).
[4] Ercan et al, Brain, 139(5):1447-1457 (2016).
[5] Gudi et al, Front Cell Neurosci 8(73) (2014).
[6] Ligneul et al, MRM, 77(4):1390-1398 (2017).
[7] Orije et al, NeuroImage, 114:128–135 (2015).

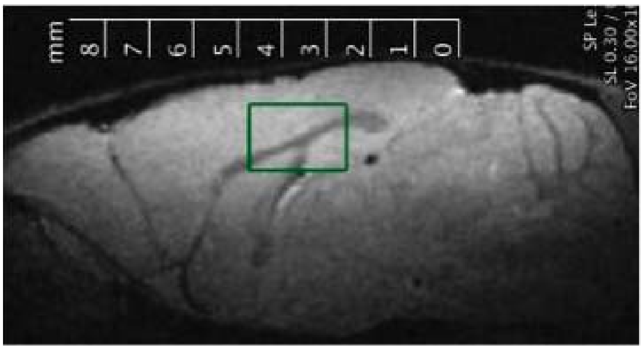

Figure 1. Location of the VOI in CC shown on a sagittal view of a T2-weighted image.

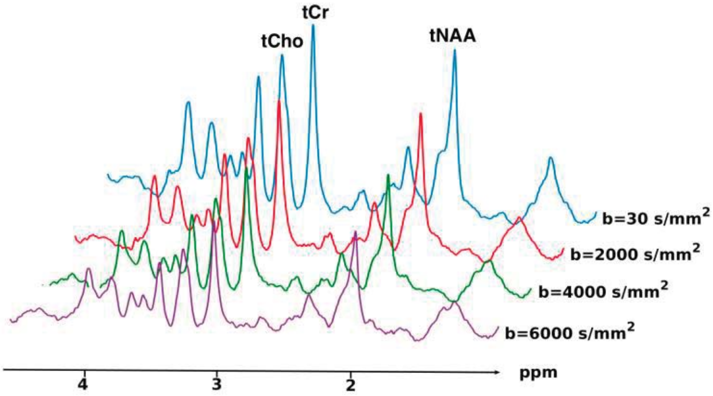

Figure 2. Examples of spectra acquired from one CPZ mouse at different b-values. The peaks corresponding to choline compounds (tCho), creatine + phosphocreatine (tCr) and N-acetylaspartate + N-acetylglutamate (tNAA) are explicitly reported.

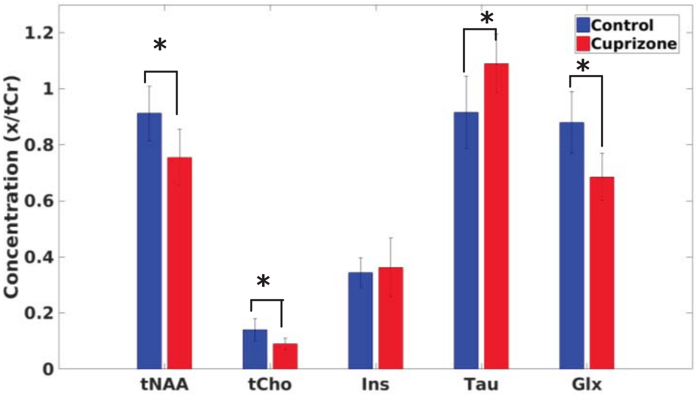

Figure 3. Mean metabolite concentration ratios relative to tCr represented with standard deviation. Statistically significant differences between CPZ and healthy mice shown with *p<0.005.

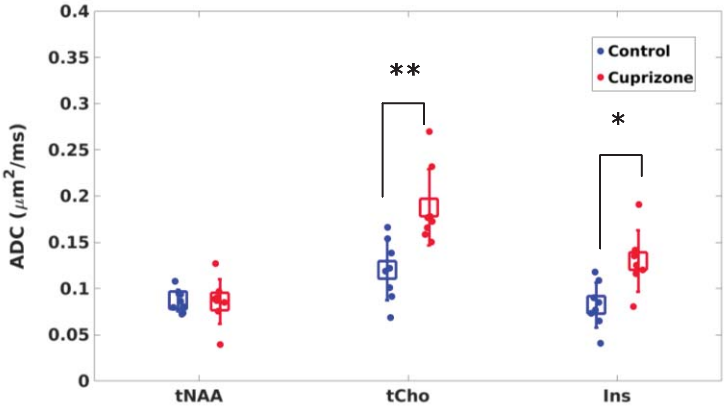

Figure 4. Box plot of the ADCs of tNAA, tCho and Ins measured from all mice (red dots CPZ mice and blue dots healthy mice). Mean ADCs (square markers) represented with standard deviation. Statistically significant differences between CPZ and healthy mice shown with *p<0.01 and **p<0.005.

Assessing tumor development with quantitative ultrasound and immunohistochemistry

Jérôme GRIFFON[1], Delphine LE GUILLOU-BUFFELLO[1], Michele LAMURAGLIA[1,2], Lori BRIDAL[1]

[1]Laboratoire d'Imagerie Biomedicale, France

[2]Medical Oncology, AP-HP, Beaujon Hospital, France

Introduction

Noninvasive, widely-accessible and standardized techniques for image acquisition and analysis are necessary to more fully evaluate heterogeneous changes in murine tumor models during growth and therapy. This work presents ultrasonic techniques to evaluate tumor size, elastic properties and functional microvascular flow as well as analysis of whole-slide fluorescent immunohistochemical markers to provide invasive reference measurements of the tumors' microstructure.

Material and Methods

An ectopic model of murine colorectal carcinoma (CT26) was implanted in 49 mice (BALB/c) on Day 0. Data were acquired from randomized groups of the mice on Day 7 (n = 10), Day 10 (n = 10), Day 14 (n = 10), Day 16 (n = 9) and Day 17 (n = 10). First, each tumor was imaged in conventional B-mode along its major, transverse and longitudinal axes and then, along the major longitudinal axis, shear-wave elastography data (SWE; SSI, Aixplorer, SL 15-4 probe) and contrast-enhanced ultrasound data (CEUS; Sequoia 512, 7-14 MHz probe, cadence contrast pulse sequencing) were acquired after a syringe-pump controlled bolus injection of 40 µL of SonoVue (Bracco Suisse, Geneva Switzerland) in the caudal vein. The ellipsoidal volume of each tumor was estimated based on the width and thickness in the major longitudinal and transversal, B-mode planes. Quantitative maps of the tissue stiffness were provided by the SSI system and saved in Dicom format. On the saved SWE data, mean and standard deviation of the SWE were calculated on the region delimiting the whole tumor on the corresponding B-mode image. CEUS sequences were saved in Dicom format. Average contrast intensity in the vascularized zone of the tumor vs. time was fit with a lognormal model to estimate the Area Under the Curve (AUC), Peak Enhancement (PE), Time to Peak (TTP), Mean Transit Time (MTT), Wash In Rate (WIR) and Wash Out Rate (WOR).

After imaging, euthanasia was administered and tumors were excised and frozen with liquid nitrogen in an Optimal Cutting Temperature compound cube and stored at -80°C. Tumors were marked to conserve orientation and approximate position relative to the US imaging plane. Slices of the tumor were cut with a cryostat (CM3050, Leica) along the largest plan and had a thickness of 10 µm. Whole-slice histological sections were then prepared with fluorescent immunohistochemical markers for reference assessment of cell nuclei (DAPI), T lymphocyte (antibody CD3 - Alexa 647), apoptosis (antibody anti-caspases 3 - TRITC) and vascular endothelium (antibody isolectine B4 - Alexa 488). These marked slices were then scanned (Axio Scan Z1, ZEISS) with a resolution of 0.325 x 0.325 µm to provide whole-slice assessment. The regions of tumor in each histological section that were free of artifacts were analyzed using in-house software to estimate the percent area of nuclei (NU), the Number of T Lymphocyte per mm² (NTL), the percent area of Apoptosis (AP) and percent area of Vascular Endothelium (VE) marker in the whole section.

Results

Parametric maps of the tumors obtained at different stages of tumor development will be presented. The evolution of the value of the parameters per day has been investigated using the non-parametric Wilcoxon rank test. For the volume, there was a significant ($p<0.01$) difference between initial (D7 and D10) and later (D14, D16, D17) days of tumor growth. The SD-SWE also showed significant ($p < 0.01$) difference between initial (D7) and later (D14, D16, D17) days, and SD-SWE was well correlated with tumor volume (RS = 0.65 [$p < 0.001$], non-parametric Spearman correlation coefficient). For the CEUS, four parameters (AUC, TTP, WIR and WOR) changed significantly between D7 and D17 and only the TTP correlated with tumor volume (RS = 0.62 [$p < 0.001$]). Mean values representing structure densities as assessed from histological data did not vary significantly over time and only a very modest variation was observed for the spatial SD or the nuclei between D10 and D17 ($p< 0.05$).

Discussion/Conclusion

No correlation between SWE and CEUS parameters was identified. Parameters related to CEUS and spatial variability of the SWE were sensitive to changes occurring within the tumors as they grew, but results did not reveal significant links between the image-based indexes and average microstructural parameters evaluated on histological data. Comparison between measurements made with the different modalities could potentially be improved by more fully sampling the tumor volume so that matched zones could better be identified.

INHA: Institut national d'histoire de l'art - Paris